ISSN 0915-633X

NATIONAL INSTITUTE FOR FUSION SCIENCE

Dynamo Mechanism in a Rotating Spherical Shell: Competition between Magnetic Field and Convection Vortices

N. Ishihara and S. Kida

(Received - June 25, 2001)

NIFS-708 July 2001

RESEARCH REPORT
NIFS Series

TOKI, JAPAN

Dynamo Mechanism in a Rotating Spherical Shell:
Competition between Magnetic Field and Convection Vortices

Norio ISHIHARA & Shigeo KIDA[1)]

Department of Physics, Nagoya University, Nagoya 464-8602, Japan
[1)] Theory and Computer Simulation Center, National Institute for Fusion Science, 322-6 Oroshi-cho, Toki, 509-5292, Japan

Key words: MHD dynamo, convection vortex, rotating spherical shell

Abstract

A strong axial magnetic dipole field having the magnetic energy 15 times larger than the kinetic of thermal convection is realized by a direct numerical simulation of the magneto-hydrodynamic equation of an electrically conducting Boussinesq fluid in a rotating spherical shell which is driven by a temperature difference between the outer and inner boundaries against a gravity force pointed to the system center. Cyclonic and anti-cyclonic convection vortices, which rotate, respectively, in the same and opposite directions of the system rotation, are generated and play a primary role in the magnetic field intensification. The magnetic field is enhanced through the stretching of magnetic lines of force in four particular places of the convection fields, namely, inside anti-cyclones, between cyclones and their western neighbouring anti-cyclones at middle as well as low latitudes, and between anti-cyclones and the outer boundary. A 'twist-turn' loop of intense magnetic flux density is identified as a fundamental structure which yields the dominant contribution both to the toroidal and poloidal components of the longitudinal averaged magnetic field. Various types of competitive interaction between magnetic field and convection vortices are observed. Among others, a creation-and-annihilation cycle of them in the statistically equilibrium state is particularly important, which is composed of three sequentially recurrent dynamical processes, that is, the generation of convection vortices by the Rayleigh-Bénard instability, the growth of anti-cyclones and the intensification of magnetic field by concentrate-and-stretch mechanism, and the break-down of vortices by the Lorentz force followed by diminution of magnetic field. The energy transfer from the velocity to the magnetic fields is taking place predominantly in this dynamical cycle.

1 Introduction

It is well known that celestial bodies have their intrinsic magnetic fields. Most planets in the solar system have dipolar fields whose axes are nearly parallel to their rotation axes, e.g. for the Earth and Jupiter, or are much inclined, e.g. for Uranus and Neptune. It is widely believed that the origin of these magnetic fields should be attributed to the dynamo action by electrically conducting fluids in their interiors (see Busse 2000, Zhang & Schubert 2000. Roberts & Glatzmaier 2001, for recent reviews). In the case of the Earth, for example, the north-south symmetry of the magnetic field structure at the core-mantle boundary (Gubbins & Bloxham 1987) together with the Taylor-Proudman theorem, which states a tendency of two-dimensionalization of fluid motions in a rotating system, strongly suggests that the dynamo action due to convective motions of electrically conducting fluids in the outer core may be responsible for generation of the geomagnetic field.

Since a suggestion of this dynamo concept by Larmor (1919), the motion of an electrically conducting fluid and the generation of magnetic field by it in a rotating spherical shell as well as in a rotating sphere have been extensively studied both theoretically and numerically. Most of the studies are based upon the magneto-hydrodynamic (MHD) equations of either an incompressible or compressible fluid. As for simulation study, recent rapid developments of computer power, numerical algorisms, and visualization techniques have made it possible to increase the available size of numerical simulation and to raise the quality of data analysis year by year. However, even now, it is still far away from a realistic direct numerical simulation of the geodynamo because of extremely large values of the control parameters such as the Taylor number and the Rayleigh number (Merill, McElhinny & McFadden 1996, Glatzmaier & Roberts 1997).

In this situation there may be at least two approaches in the dynamo simulation study. One is to stick to the original purpose to get a numerical solution which agrees *quantitatively* with observations of the geomagnetic field. For such an ambition, however, the basic equations, such as the MHD equations, are too heavy to be solved. It is necessary, therefore, to lighten the computation load by introducing some insightful simplifications, e.g. by asymptotic analyses, by phenomenological arguments, and by elaborate numerical methods. In fact, some characteristic behaviours of the geodynamo, such as the dominance of dipolar field having reasonable magnitude and a reversal of its polarity have been successfully realized by the use of variants of the MHD equations either with hyper-diffusion coefficients, without the inertial term, or under slip boundary condition (e.g. Glatzmaier & Roberts 1995, Kuang & Bloxham 1997). The other approach is to concentrate our attention on understanding of a fundamental process of the convection dynamo in a rotating spherical shell. Closeness of the values of control parameters is then not strongly required between the dynamical system and the real Earth or any celestial bodies. Similar (but different in the type of viscosity, fluid compressibility, numerical scheme, boundary condition, etc.) convection dynamo simulations in a rotating spherical shell have been performed by several research groups independently to realize also some characteristics of the geodynamo at least *qualitatively* (e.g. Kageyama &

Sato 1997, Kitauchi & Kida 1998, Katayama, Matsushima & Honkura 1999, Sakuraba & Kono 1999, Olson, Christensen & Glatzmaier 1999).

We have learned a lot, from these extensive simulations, on the global structure and behaviour of the convection velocity and magnetic fields in a rotating spherical shell, but not so much as on the dynamo mechanism itself. The averaged (e.g. over the whole longitudes) global structure of the fields are relatively easily visualized, but the instantaneous local structure, which is responsible to the dynamo action, is very hard because of unsteadiness, irregularity, and three-dimensionality of variations of the fields. As has already been recognized by many simulation studies (Kitauchi & Kida 1998, Katayama, Matsushima & Honkura 1999, Olson, Christensen & Glatzmaier 1999), the interaction between the convection velocity and magnetic fields is taking place locally in space, which implies that the generation and maintenance of magnetic fields should be local phenomena. This immediately rings a warning bell that an easy average, such as a longitudinal average, may loose some important dynamics of local nature. For example, the $\alpha\omega$ dynamo, if it is argued on the bases of only the longitudinal averaged quantities may miss the true mechanism of local nature and lead to a misleading conclusion. It should be stressed here that a detailed analysis, without any averages, of the individual local dynamical process is indispensable to capture the real physics.

The second approach stated above are taken here. We solve the MHD equations as accurately as possible for an incompressible Boussinesq fluid of constant material parameters confined in a rotating spherical shell with uniform constant temperature distribution on the boundaries under a gravity force pointed to the system center. This is one of the simplest non-trivial settings to study the dynamo mechanism which imitates spherical celestial bodies. Our primary interest is to find a possible mechanism of some characteristics observed in the geomagnetic field such as the dominance of a dipole magnetic field with axis nearly parallel to the rotation axis, the intermittent irregular reversals of the dipole polarity, the spottiness of intensified magnetic field, the westward drift, and so on, under the dynamo action by convection motions of an electrically conducting fluid. We assume that three factors, [1] the system rotation, [2] the spherical boundary, and [3] the convective motion of an electrically conducting fluid, are fundamental to produce the above-mentioned characteristics. Other factors, such as the inner core (Glatzmaier & Roberts 1995, Hollerbach & Jones 1995, Sakuraba & Kono 1999), fluid compressibility (Kageyama & Sato 1997), the source of convection motion, e.g. the latent heat and the compositional buoyancy (Glatzmaier & Roberts 1996), are assumed to give the secondary effects and not taken into consideration in the present analysis.

In this paper we analyze a run which exhibits an axial dipole field (Ishihara & Kida 2000) to examine the dynamo mechanism. We find strong competitive interactions between magnetic field and convection vortices, in which dynamo action is taking place. In the next section a numerical model of thermally driven MHD dynamo problem in a rotating spherical shell is introduced with fundamental equations, governing parameters, initial and boundary conditions, and numerical schemes. A purely thermal convection simulation is described in §3. Then, a dynamo simulation follows. In §4, the dynamics of global quantities, such as the energy and the magnetic dipole moment are discussed. In §5, the intensification mechanism of the mag-

netic field is presented. There are three distinct periods of temporal evolution of the magnetic field, i.e. the linear, first-equilibrium and second-equilibrium periods. After the dynamo mechanisms in the respective periods are described in detail, an overview of the most intensified places of the magnetic field is taken. Then, we discuss, in §6, a competitive interaction — a creation-and-annihilation cycle of magnetic field and convection vortices. Finally, section seven is devoted for further remarks and conclusions.

2 Spherical-Shell Model

We consider the magnetic field intensification by thermal convection of an electrically conducting fluid between two concentric spheres which are rotating with the same constant angular velocity $\boldsymbol{\Omega}$ around the center. The density ρ of the fluid is assumed to be uniform and constant except in the buoyancy force term. This is the so-called Boussinesq approximation. The inside of the inner sphere and the outside of the outer sphere are assumed to be vacuum with the same magnetic permeability μ as that of the fluid, for simplicity. A gravity force $\boldsymbol{g}$ per unit volume acting on fluid elements is directed to the system center and is proportional to the distance from the center, i.e. $\boldsymbol{g} = -\rho\gamma\boldsymbol{x}$, where γ is a constant and $\boldsymbol{x}$ is a position vector relative to the center. The temperature is kept uniform over the two boundary spheres and constant at all times. The inner sphere is hotter than the outer by ΔT, which drives a thermal convection. Two coordinate systems, the Cartesian (x, y, z) and the spherical (r, θ, ϕ), with the origin at the center are used as the case may be. The (x, y) plane is taken on the equatorial plane and the z axis on the rotation axis, whereas r is the radial, θ is the co-latitudinal, and ϕ is the longitudinal coordinates. In the following we use such coordinates systems rotating either with the spherical shell or with the vortex columns according to circumstances.

The dynamical equations, in a frame rotating with the shell, for the fluid velocity $\boldsymbol{u}(\boldsymbol{x}, t)$, the magnetic flux density $\boldsymbol{b}(\boldsymbol{x}, t)$, and the temperature $T(\boldsymbol{x}, t)$ are given by the Navier-Stokes equation,

$$\frac{\mathrm{D}\boldsymbol{u}}{\mathrm{D}t} = \underbrace{-\nabla\left(\frac{p}{\rho} + \frac{1}{2}\gamma|\boldsymbol{x}|^2 - \frac{1}{2}|\boldsymbol{\Omega}\times\boldsymbol{x}|^2\right)}_{\text{pressure}} + \underbrace{\mathrm{PrRa}T\boldsymbol{x}}_{\text{buoyancy}} + \underbrace{\mathrm{PrTa}^{\frac{1}{2}}\boldsymbol{u}\times\widehat{\boldsymbol{z}}}_{\text{Colioris}} + \underbrace{(\nabla\times\boldsymbol{b})\times\boldsymbol{b}}_{\text{Lorentz}} + \underbrace{\mathrm{Pr}\nabla^2\boldsymbol{u}}_{\text{viscous}}, \tag{1}$$

the electro-magnetic induction equation,

$$\frac{\mathrm{D}\boldsymbol{b}}{\mathrm{D}t} = (\boldsymbol{b}\cdot\nabla)\boldsymbol{u} + \mathrm{Ro}\nabla^2\boldsymbol{b}, \tag{2}$$

and the heat conduction equation,

$$\frac{\mathrm{D}T}{\mathrm{D}t} = \nabla^2 T. \tag{3}$$

Since the fluid is incompressible and there is no magnetic mono-pole, both the velocity and magnetic fields are solenoidal,

$$\nabla\cdot\boldsymbol{u} = 0 \tag{4}$$

and

$$\nabla \cdot \boldsymbol{b} = 0. \tag{5}$$

Here, $p(\boldsymbol{x}, t)$ is the pressure, $\widehat{\boldsymbol{z}} = \boldsymbol{\Omega}/|\boldsymbol{\Omega}|$ is the unit vector along the rotation axis, and

$$\frac{\mathrm{D}}{\mathrm{D}t} = \frac{\partial}{\partial t} + (\boldsymbol{u} \cdot \nabla) \tag{6}$$

is the Lagrangian derivative. All the variables have been normalized in terms of the shell thickness d $(= r_2 - r_1)$, where r_1 and r_2 are the radii of the inner and outer spheres, the thermal diffusion time d^2/κ (κ being the thermal diffusivity), and the characteristic magnetic flux density $\kappa(\mu\rho)^{\frac{1}{2}}/d$. There appear four dimensionless parameters in these equations, which are the Prandtl number,

$$\mathrm{Pr} = \frac{\nu}{\kappa}, \tag{7}$$

the Rayleigh number,

$$\mathrm{Ra} = \frac{\alpha\gamma\Delta T d^4}{\kappa\nu}, \tag{8}$$

the Taylor number,

$$\mathrm{Ta} = \left(\frac{2|\boldsymbol{\Omega}|d^2}{\nu}\right)^2, \tag{9}$$

and the Roberts number,

$$\mathrm{Ro} = \frac{\lambda}{\kappa}, \tag{10}$$

where α is the thermal expansion coefficient of fluid, ν is the kinematic viscosity, and λ is the electrical resistivity.

These equations are solved numerically under the boundary conditions that the velocity vanishes, the magnetic field is continuous,[1] and the temperature is uniform and constant on both the inner and outer spheres. Simulations are performed by the pseudo-spectral method. All the dependent variables are expanded by the spherical harmonics on the latitudinal and longitudinal directions and by the Chebyshev polynomials in the radial direction. Simultaneous ordinary differential equations with respect to time for the expansion coefficients are solved by the Crank-Nicolson scheme for the diffusion terms and by the second-order Adams-Bashforth scheme for the other terms (Kitauchi, Araki & Kida 1997).

Our primary interest here is to understand how the magnetic field is intensified through mutual interactions with the thermal convection generated by a steady and uniform temperature difference between the outer and inner boundaries of a rotating spherical shell. For this

[1]This is the condition that there is no surface current, which is compatible with a finite electrical resistivity and in contrast with the vanishing Poynting flux which requires an unphysical infinite surface current (Kageyama & Sato 1997).

purpose we solve the initial value problem of (1)-(5) in two steps. First, eqs. (1), (3), and (4) with $\boldsymbol{b} \equiv \boldsymbol{o}$ are simulated starting with thermal conduction state,

$$\boldsymbol{u} = \boldsymbol{o}, \qquad T = \frac{r_1}{r_2 - r_1}\left(\frac{r_2}{r} - 1\right) \tag{11}$$

superimposed by random disturbances both in the velocity and temperature fields. The Taylor number, the Prandtl number, and the radius ratio of the two spheres are respectively set at

$$\mathrm{Ta} = 1.6 \times 10^6, \qquad \mathrm{Pr} = 1, \qquad \frac{r_1}{r_2} = 0.5. \tag{12}$$

These values are chosen as an extension of a series of our previous studies (Kida, Araki & Kitauchi 1997, Kida & Kitauchi 1998a, 1998b, Kitauchi & Kida 1998), namely, the Taylor number is increased by factor 4 under the expectation that more intensified magnetic field may be generated. The critical Rayleigh number in the linear stability of thermal conduction state (11) at these parameters is found to be $\mathrm{Ra}_c = 1.36 \times 10^4$. A thermal convection state develops at a super-critical Rayleigh number. Simulations for several cases of different Rayleigh numbers were performed. Here, we report a case of

$$\mathrm{Ra} = 3.2 \times 10^4, \tag{13}$$

in which a strong axial magnetic dipole filed is developed (Ishihara & Kida 2000). Since the Rayleigh number is quite away from the critical value ($\mathrm{Ra}/\mathrm{Ra}_c = 2.4$) the resulting thermal convection is rather irregular both in space and time (cf. figure 4 in Busse 2000).

In the second step of the simulation a random seed of weak magnetic field is sowed in a thermal convection state obtained in the first step, and the temporal evolutions of the magnetic and velocity fields are traced by solving the full set of MHD equations (1)-(5). Whether the magnetic intensification is effective or not depends on the Roberts number. It is found that the magnetic field is intensified when it is below the critical value $\mathrm{Ro}_c = 0.149$. In the following we present the results at

$$\mathrm{Ro} = 0.1. \tag{14}$$

The numbers of modes in the simulation are taken as $(N_r, N_\theta, N_\phi) = (128, 64, 128)$ in the radial, latitudinal and longitudinal directions, where N_r is the number of terms in the Chebyshev polynomial expansions, and N_θ and N_ϕ are the truncation orders in the spherical harmonic expansion. It turns out that these truncation orders may be large enough to guarantee the numerical accuracy in the sense that the peak value of the power spectra of the dependent variables drop by a factor of $10^{-2} \sim 10^{-3}$ at the cut-off mode even when the magnetic energy is highest in the present numerical simulation (cf. Christensen, Olson & Glatzmaier 1999). The time step width is $\Delta t = 1.25 \times 10^{-5}$. The magnetic, viscous, and thermal diffusion times are $d^2/\lambda = 10$, $d^2/\nu = 1$, and $d^2/\kappa = 1$, respectively.

In the following sections we will analyze the interaction of the velocity and magnetic fields in terms of various physical quantities, including vorticity $\boldsymbol{\omega}(\boldsymbol{x}, t) = \nabla \times \boldsymbol{u}(\boldsymbol{x}, t)$. For later

convenience, we write here the evolution equation of vorticity, which is obtained by taking a curl of the Navier-Stokes equation (1), as

$$\frac{\mathrm{D}\boldsymbol{\omega}}{\mathrm{D}t} = \underbrace{(\boldsymbol{\omega}\cdot\nabla)\boldsymbol{u}}_{\text{stretching}} + \underbrace{\mathrm{PrRa}(\nabla T)\times\boldsymbol{x}}_{\text{buoyancy}} + \underbrace{\mathrm{PrTa}^{\frac{1}{2}}\frac{\partial \boldsymbol{u}}{\partial z}}_{\text{Colioris}} + \underbrace{\nabla\times(\boldsymbol{j}\times\boldsymbol{b})}_{\text{Lorentz}} + \underbrace{\mathrm{Pr}\nabla^2\boldsymbol{\omega}}_{\text{diffusion}}, \tag{15}$$

where $\boldsymbol{j}(\boldsymbol{x},t) = \nabla\times\boldsymbol{b}(\boldsymbol{x},t)$ is the current density. The physical meanings of the five terms on the right-hand side are respectively the stretching and tilting of vorticity by advection, the torque by buoyancy force, the stretching and tilting of system vorticity ($2\boldsymbol{\Omega}$) by advection, the torque by Lorentz force, and the diffusion by viscosity. See Kitauchi & Kida (1998) for details.

3 Structure of Thermal Convection

As described in the preceding section, the velocity field which causes the magnetic field intensification is prepared by a pure thermal convection simulation. Therefore, it is instructive to see the characteristic properties of the structure of this thermal convection for discussion of the intensification mechanism. The structure is not so simple as might be expected from the geometry and the boundary condition of the problem. A competition between two different symmetries, i.e. the spherical symmetry of the boundaries and the cylindrical symmetry of the system rotation, makes the flow very complicated (Kitauchi, Araki & Kida 1997). Although the details are different depending on the three parameters of (12), the overall flow structure can be understood by the Taylor-Proudman vortex columns of alternated senses of rotation around the axis of system rotation.

An instantaneous flow structure in the fully developed thermal convection state is shown in figure 1. The iso-surfaces of $|\boldsymbol{\omega}|$ are drawn with yellow for cyclones ($\omega_z > 0$) and blue for anti-cyclones ($\omega_z < 0$) in (a). The threshold value $|\boldsymbol{\omega}|$ is the same on all the surfaces. This is a view seen from 30^o north latitude. The gray circular annulus represents the equatorial plane and the sphere at the center the inner boundary of the spherical shell. The outer boundary is omitted. There are nine cyclonic and anti-cyclonic columns aligned alternately around the rotation axis. Besides these vortex columns the so-called Ekman boundary layers develop on the outer and inner spheres where vorticity is parallel to the boundaries and very intense. The thickness of the Ekman boundary layers on the inner and outer spheres is nearly the same and about $0.06d$ which is covered by 20 Chebyshev points in the numerical scheme, implying that these boundary layers are well resolved. The Ekman boundary layers are cut away in these figures to make the inside of the shell visible. The z component of vorticity dominates the other components except in the Ekman boundary layers. The size and shape of iso-surfaces are different from vortex to vortex and change in time rather irregularly. Their intensity is not uniform along the axis. It is more intense near the outer boundary in cyclones, whereas near the equatorial plane in anti-cyclones. The vortices retrograde with mean angular velocity of $\Omega_{TP} = -0.9\ (= -0.01\Omega)$.

The velocity field in the whole spherical shell is genuinely three-dimensional and more complicated than the vorticity field. However, the key structure, which is important for the

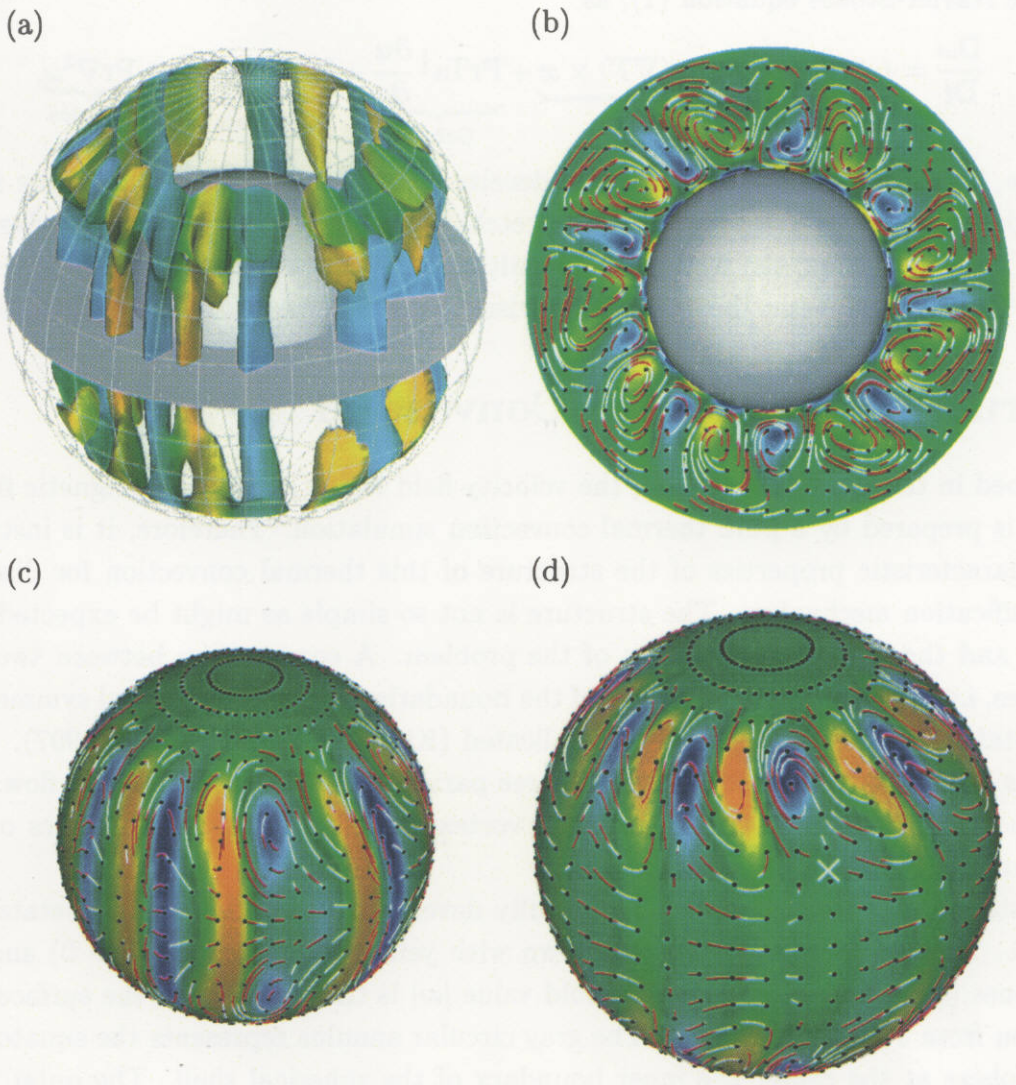

Figure 1: Thermal convection. (a) Iso-surfaces of $|\boldsymbol{\omega}|$ are drawn with yellow for cyclones ($\omega_z > 0$) and blue for anti-cyclones ($\omega_z < 0$). (b) Equatorial distribution of ω_z and streamlines. The colour map represents ω_z with yellow for positive and blue for negative. (c) Streamlines projected on a sphere of radius $r = r_1 + 0.55d$ (r_1 being the inner-sphere radius and d the shell thickness) on which the magnetic field is intensified strongly in the linear period (see figures 7(a) and 8). The colour map represents u_r with blue for positive and yellow for negative. (d) Same as figure (c) but on a sphere of radius $r = r_1 + 0.92d$ just outside of the Ekman boundary layer on the outer sphere. A white cross denotes a stagnation point. Figures (a), (c), and (d) are viewed from 30° north latitude. The streamlines in (b)-(d) refer to the velocity field in a frame moving with the convection vortices. Streamlines are shown by coloured lines with black circles toward which the flow is pointed. The velocity magnitude is proportional to the line length. Red and white denote the positive and negative accelerations on the lines.

magnetic field intensification, is relatively easily pictured by recalling the properties of the Taylor-Proudman vortex columns and the Ekman boundary layers. The cyclones (or anti-cyclones) are vortices of high- (or low-) pressure with swirling flows in the same (or opposite) sense as the rotation of the spherical shell and with axial flows toward (or away from) the equatorial plane, which is caused by the Colioris force and the Ekman pumping. Therefore, the flows inside both the cyclones and anti-cyclones are helical and skewed as a left-handed (or a right-handed) screw in the northern (or southern) hemisphere (Kitauchi, Araki & Kida 1997). The flow pattern on the equatorial plane is simpler because the velocity field is of mirror symmetry at least approximately. The structures of the velocity and vorticity fields on the equatorial plane are shown in figure 1(b), where red-and-white lines with a black circle represent streamlines projected on this plane relative to a frame moving with the vortex columns. The velocity is directed to the circle and the acceleration is positive and negative at red and white, respectively. The line length is proportional to the velocity magnitude. The colour map represents ω_z with red, green, and blue for the positive, zero, and negative values, respectively. The flow is spiralling out of (or into) the cyclones (or anti-cyclones). This is consistent with the flows leaving from (or approaching to) the equatorial plane in the cyclones (or anti-cyclones). The anti-cyclones are stronger and concentrated in space more than the cyclones. As will be shown in §§5.2 and 5.3, the magnetic field is intensified by the concentrate-and-stretch mechanism of magnetic lines of force in anti-cyclones (Kitauchi & Kida 1998).

Two other flow patterns important for the magnetic field intensification are shown in figures 1(c) and (d) on spheres of radii $r = r_1 + 0.55d$ and $r_1 + 0.92d$, respectively. Here, the notation of streamlines is the same as in figure 1(b), whereas the colour map represents the radial component u_r of velocity with yellow for $u_r < 0$ and blue for $u_r > 0$. As will be seen later, the magnetic field is most intensified around these spheres (see Table 1). The flow is swirling clockwise (or anti-clockwise) around cyclones (or anti-cyclones) and sinking into (or going out of) the Ekman boundary layer. Therefore the streamlines are skewed in the same sense as a left-handed screw in the northern hemisphere. Note that the yellow and blue in figure 1(d) represent the cyclones and anti-cyclones in just the same manner as in figure 1(a).

The important point to notice in magnetic field intensification is that the acceleration is positive at the inner (or outer) side between a cyclone and an eastern (or a western) neighbouring anti-cyclone. In §5.1, the magnetic field is shown to be intensified at the place of positive acceleration by the stretching of magnetic lines of force. There is a stagnation point, denoted by a white cross, to the south of an anti-cyclone around which the flow is being stretched in the direction of the north-west and the south-east. As will be shown in §5.2, the magnetic field is also intensified along this flow.

4 Growth of Magnetic Field

The second step of the simulation described in §2 is performed by sowing a seed of random weak magnetic field in a thermal convection obtained in the preceding section. Initially, the

Lorentz force is negligible in the Navier-Stokes equation (1) so that there is no feedback effect on the velocity field, and the induction equation (2) is linear with respect to the magnetic flux density. Since the velocity field is stationary in the statistical sense, the intensity of the magnetic field should change exponentially in time. The growth rate is a decreasing function of the Roberts number. The critical Roberts number is found to be 0.149, below which the magnetic field is intensified. In the following we report a case of $\mathrm{Ro} = 0.1$.

4.1 Energy equations

The convection dynamo is, after all, the energy transfer from the convective motion excited by a temperature difference between the inner and outer boundaries to the magnetic field. Therefore, the examination of the energy flow is useful to understand the dynamo mechanism.

The temporal evolution of the kinetic energy density per unit mass $\frac{1}{2}|\boldsymbol{u}|^2$ is derived by taking the inner product of (1) and $\boldsymbol{u}$ as

$$\frac{\mathrm{D}}{\mathrm{D}t}\frac{1}{2}|\boldsymbol{u}|^2 = \underbrace{-\nabla\cdot\boldsymbol{u}\left(\frac{p}{\rho}+\frac{1}{2}\gamma|\boldsymbol{x}|^2-\frac{1}{2}|\boldsymbol{\Omega}\times\boldsymbol{x}|^2\right)}_{\text{diffusion by pressure}} + \underbrace{\mathrm{PrRa}T\,\boldsymbol{x}\cdot\boldsymbol{u}}_{\text{buoyancy}} + \underbrace{\boldsymbol{u}\cdot(\boldsymbol{j}\times\boldsymbol{b})}_{\text{Lorentz}} + \underbrace{\mathrm{Pr}\boldsymbol{u}\cdot\nabla^2\boldsymbol{u}}_{\text{viscous}}. \tag{16}$$

The first term on the right-hand side represents the diffusion of the kinetic energy density by the pressure, the gravity force, and the centrifugal force, which is integrated out over the spherical shell because of no-slip boundary conditions. The second term expresses the buoyancy effects which is the only source of the kinetic energy. The third term is the work done by the Lorentz force which is responsible to the direct energy exchange between the convection velocity and magnetic fields. The sign of this term turns out to be negative, which implies that the kinetic energy is converted to the magnetic. The last one includes all the contribution from the viscous effects, which may be written in a sum of diffusion and dissipation such as $\mathrm{Pr}(\nabla^2\frac{1}{2}|\boldsymbol{u}|^2+\nabla\nabla:\boldsymbol{u}\boldsymbol{u}-2\parallel\underline{\boldsymbol{s}}\parallel^2)$ and $\mathrm{Pr}(\nabla^2\frac{1}{2}|\boldsymbol{u}|^2-\nabla\nabla:\boldsymbol{u}\boldsymbol{u}-|\boldsymbol{\omega}|^2)$. Here, $\underline{\boldsymbol{s}}=\{s_{ij}\}$, $s_{ij}=\frac{1}{2}(\partial u_j/\partial x_i+\partial u_i/\partial x_j)$, $(i,j=1,2,3)$ is the rate-of-strain tensor. In either of these decompositions the first two terms represent the diffusion, whereas the third one the dissipation. The diffusion terms are integrated out over the whole spherical shell. Note that the Colioris term does not contribute to the energy dynamics at all, though it fluctuates with substantial amplitude (see (29) below).

The evolution equation of the magnetic energy density $\frac{1}{2}|\boldsymbol{b}|^2$, on the other hand, is derived by taking the inner product of (2) and $\boldsymbol{b}$ as

$$\frac{\mathrm{D}}{\mathrm{D}t}\frac{1}{2}|\boldsymbol{b}|^2 = \underbrace{\boldsymbol{b}\cdot\underline{\boldsymbol{s}}\cdot\boldsymbol{b}}_{\text{stretching}} + \underbrace{\mathrm{Ro}\,\boldsymbol{b}\cdot\nabla^2\boldsymbol{b}}_{\text{resistive}}. \tag{17}$$

The first term on the right-hand side of (17) contributes to the growth (or decay) of the magnetic energy density by stretch (or contract) of the magnetic lines of force. The interrelation between directions of the magnetic lines of force and of the eigenvector with positive eigenvalues

of the rate-of-strain tensor is especially important for the magnetic field intensification. The second term describes the effects of resistivity, which may be rewritten as a sum of diffusion and dissipation, e.g. $\mathrm{Ro}(\nabla \cdot (\boldsymbol{b} \times \boldsymbol{j}) - |\boldsymbol{j}|^2)$. In this decomposition the first term represents the diffusion, whereas the second the dissipation by the Joule heating. In fact, the magnetic field in vacuum outside the spherical shell is excited through this diffusion term (see §4.2).

Another expression of the evolution of the magnetic energy density is

$$\frac{\partial}{\partial t}\frac{1}{2}|\boldsymbol{b}|^2 = -\underbrace{\boldsymbol{u} \cdot (\boldsymbol{j} \times \boldsymbol{b})}_{\text{Lorentz}} - \underbrace{\nabla \cdot (\boldsymbol{E} \times \boldsymbol{b})}_{\text{Poynting}} - \underbrace{\mathrm{Ro}|\boldsymbol{j}|^2}_{\text{Joule}}, \tag{18}$$

where

$$\boldsymbol{E} = \mathrm{Ro}\boldsymbol{j} - \boldsymbol{u} \times \boldsymbol{b} \tag{19}$$

is the normalized electric field. The respective terms on the right-hand side of (18) represent the reaction of the Lorentz force, the electro-magnetic energy flux due to the spatial variation of Poynting vector $\boldsymbol{E} \times \boldsymbol{b}$, and the Joule heating.

Two equivalent equations (17) and (18), which are, so to speak, the fluid dynamical and the electro-magnetic representations, respectively, yield different descriptions of the energy dynamics. We use the fluid dynamical representation (17) throughout this paper.

4.2 Energy dynamics

The magnitude of variations of the velocity and magnetic fields is conveniently measured by the kinetic energy,

$$\mathcal{E}_K(t) = \tfrac{1}{2}\int_{V_{\mathrm{shell}}} |\boldsymbol{u}|^2 \, \mathrm{d}V \tag{20}$$

and the magnetic energy,

$$\mathcal{E}_M(t) = \tfrac{1}{2}\int_{V_{\mathrm{all}}} |\boldsymbol{b}|^2 \, \mathrm{d}V, \tag{21}$$

where V_{all} and V_{shell} denote the whole space and the spherical shell, respectively. Note that the magnetic energy $\mathcal{E}_M(t)$ is taken from the whole space, whereas the kinetic energy $\mathcal{E}_K(t)$ is only from the inside of the shell.

The evolution equation for the kinetic energy is derived by integrating (16) over the spherical shell as

$$\frac{\mathrm{d}\mathcal{E}_K}{\mathrm{d}t} = \mathcal{Q}_B - \mathcal{Q}_L - \mathcal{Q}_V, \tag{22}$$

whereas that for the magnetic energy is derived by integrating (17) or (18) over the entire space as

$$\frac{\mathrm{d}\mathcal{E}_M}{\mathrm{d}t} = \mathcal{Q}_L - \mathcal{Q}_R. \tag{23}$$

Here,

$$\mathcal{Q}_B = \mathrm{PrRa} \int_{V_{\mathrm{shell}}} T\, \boldsymbol{x} \cdot \boldsymbol{u}\, \mathrm{d}V \tag{24}$$

is the work done by the buoyancy force,

$$\begin{aligned} \mathcal{Q}_L &= -\int_{V_{\mathrm{shell}}} \boldsymbol{u} \cdot (\boldsymbol{j} \times \boldsymbol{b})\, \mathrm{d}V \\ &= \int_{V_{\mathrm{shell}}} \boldsymbol{b} \cdot \underline{\boldsymbol{s}} \cdot \boldsymbol{b}\, \mathrm{d}V \qquad (>0) \end{aligned} \tag{25}$$

is regarded as either minus the work done by the Lorentz force or the growth rate of magnetic energy density by stretching of magnetic lines of force,

$$\begin{aligned} \mathcal{Q}_V &= \mathrm{Pr} \int_{V_{\mathrm{shell}}} |\boldsymbol{\omega}|^2 \mathrm{d}V \\ &= 2\ \mathrm{Pr} \int_{V_{\mathrm{shell}}} \| \underline{\boldsymbol{s}} \|^2\, \mathrm{d}V \end{aligned} \tag{26}$$

is the viscous dissipation, and

$$\mathcal{Q}_R = \mathrm{Ro} \int_{V_{\mathrm{shell}}} |\boldsymbol{j}|^2\, \mathrm{d}V \tag{27}$$

represents the resistive dissipation (the Joule heating). The positiveness of (25) is a result of the present numerical simulation. Thus, $\mathcal{Q}_L$ may represent the energy transfer rate from the velocity to magnetic fields. Notice that the magnetic field is being excited also in vacuum outside the spherical shell but the supply and dissipation of the magnetic energy are confined inside the shell. This implies that the magnetic energy fluxes either outward or inward through the boundaries of the spherical shell. The diffusion term (e.g. $\mathrm{Ro}\nabla \cdot (\boldsymbol{b} \times \boldsymbol{j})$ in (17) and $\mathrm{Ro}\nabla \cdot (\boldsymbol{E} \times \boldsymbol{b})$ in (18)) is responsible to it.

Energy equations (22) and (23) tell us the following scenario of the energy flux between the velocity and magnetic fields in the statistically steady state. The kinetic energy is supplied to the velocity field by the buoyancy force, a part of which is dissipated by viscosity and the rest is transferred to the magnetic field through the Lorentz force. This magnetic energy is dissipated by resistivity inside the shell. The magnetic field is also excited in vacuum outside the shell, the energy of which is typically several percent of that in the shell. A detail of the energy balance will be discussed below (see figure 3). By summing up (22) and (23), we obtain the governing equation of the total energy as

$$\frac{\mathrm{d}}{\mathrm{d}t}(\mathcal{E}_K + \mathcal{E}_M) = \mathcal{Q}_B - \mathcal{Q}_V - \mathcal{Q}_R. \tag{28}$$

In figure 2, we plot the temporal evolutions of the kinetic and the magnetic energy (a) in a semi-logarithmic scale and (b) in a linear scale. A solid and a broken line denotes the kinetic

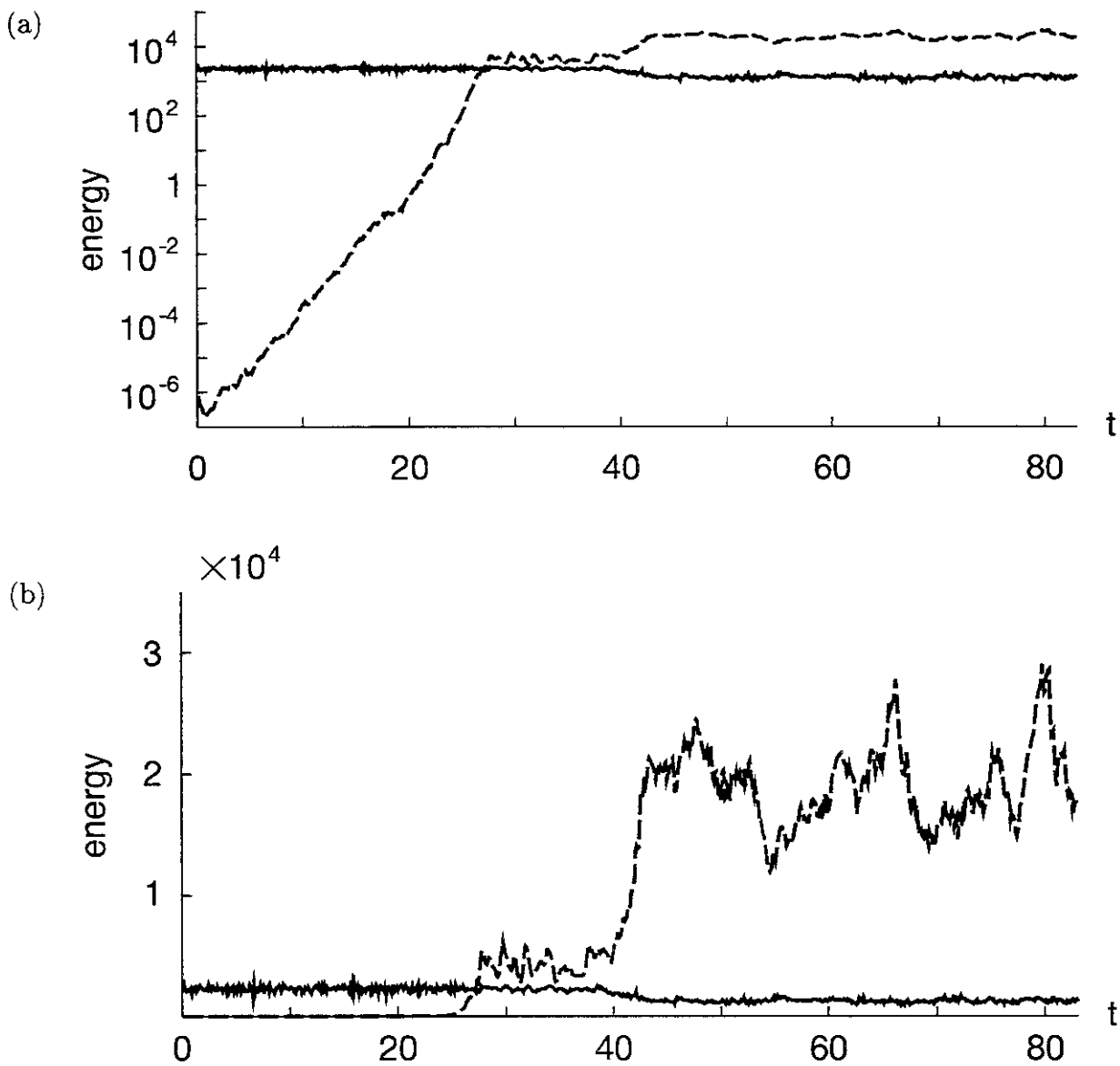

Figure 2: Temporal evolutions of the kinetic and the magnetic energy. (a) Semi-logarithmic scale. (b) Linear scale. A solid and a broken line denotes the kinetic and the magnetic energy, respectively.

and the magnetic energy, respectively. Initially, after a short transient time ($0 < t < 1$), the magnetic energy increases exponentially in time with growth rate 0.78. It exceeds the kinetic energy at $t \approx 27.1$, then stops increasing at $t \approx 28$ and fluctuates around the mean value $4,353$ until $t \approx 38$, which is about double the mean kinetic energy $2,239$. Those periods during which the magnetic energy increases exponentially and fluctuates around some level are called the 'linear period' and the 'first-equilibrium period', respectively. The kinetic energy is hardly different, in the mean, between the two periods, but the fluctuations are much larger in the earlier. A drastic change of the kinetic energy occurs at $t = 41 \sim 43$, across which the magnetic energy increases by factor 4.5, whereas the kinetic energy decreases by 43%. The period after the change is called the 'second-equilibrium period'. As seen in figure 2(b) the magnetic energy exhibits a quasi-periodic saw-tooth fluctuations in the second-equilibrium period. This is a manifestation of a creation-and-annihilation cycle of convection vortices and magnetic field which will be discussed in §6. The mean magnetic energy inside of the inner sphere is about 0.5%, 1% and 5% of the total in the linear, first-equilibrium and second-equilibrium periods, respectively. The corresponding values outside of the outer sphere are about 2%, 3% and 12%.

In order to see how the supplied energy by a temperature difference between the inner and outer spheres is transferred to the magnetic energy, we compare, in figure 3, the time series of each term in energy equations (22) and (23). Figure 3(a) shows the balance in the kinetic energy equation in which a dashed, a solid, and a dotted line denotes contributions from the buoyancy force, minus the Lorentz force, and the viscous force, respectively. Throughout the simulation period the buoyancy force always gives positive contribution which counterbalances the sum of those of the Lorentz and viscous forces. In the linear period ($t < 26$) the contributions from the buoyancy and viscous forces compete almost perfectly and the difference is less than a few percent at every instant of time. In the first- and second-equilibrium periods, on the other hand, the contribution from the Lorentz force is substantial, which is about 21% and 50% of that from the buoyancy force in the respective periods. The viscous dissipation is negative all the times, the magnitude of which hardly changes throughout the linear and first-equilibrium periods but is reduced by half in the second-equilibrium period, which coincides with the reduction of the kinetic energy (see figure 2). The contribution from the Lorentz force increases exponentially in time in the linear period, the growth rate of which is the same as that of the magnetic field. It fluctuates around a constant level in each of the first- and second-equilibrium periods and jump abruptly between the two periods. This abrupt change of the contribution from the Lorentz force is an indication of difference in the dynamo mechanism between the first- and second-equilibrium periods (see §§5.2 and 5.3 below). Another noticeable jump in $\mathcal{Q}_B$ between the linear and first-equilibrium periods, which synchronizes with the variation of $\mathcal{Q}_L$, is interesting, but we have no clear-cut explanation of it.

Figure 3(b) for the magnetic field shows that the contribution from the stretching of magnetic lines of force (which is equal to that from the Lorentz force, see (25)) balances with the resistive dissipation almost perfectly in the whole period. But there exists a small systematic time-lag between them. To see it, we compare, in figure 4, the temporal evolutions of $\mathcal{Q}_L$ (solid line) and $\mathcal{Q}_R$ (broken line) in an enlarged part of the first-equilibrium period. Their variations

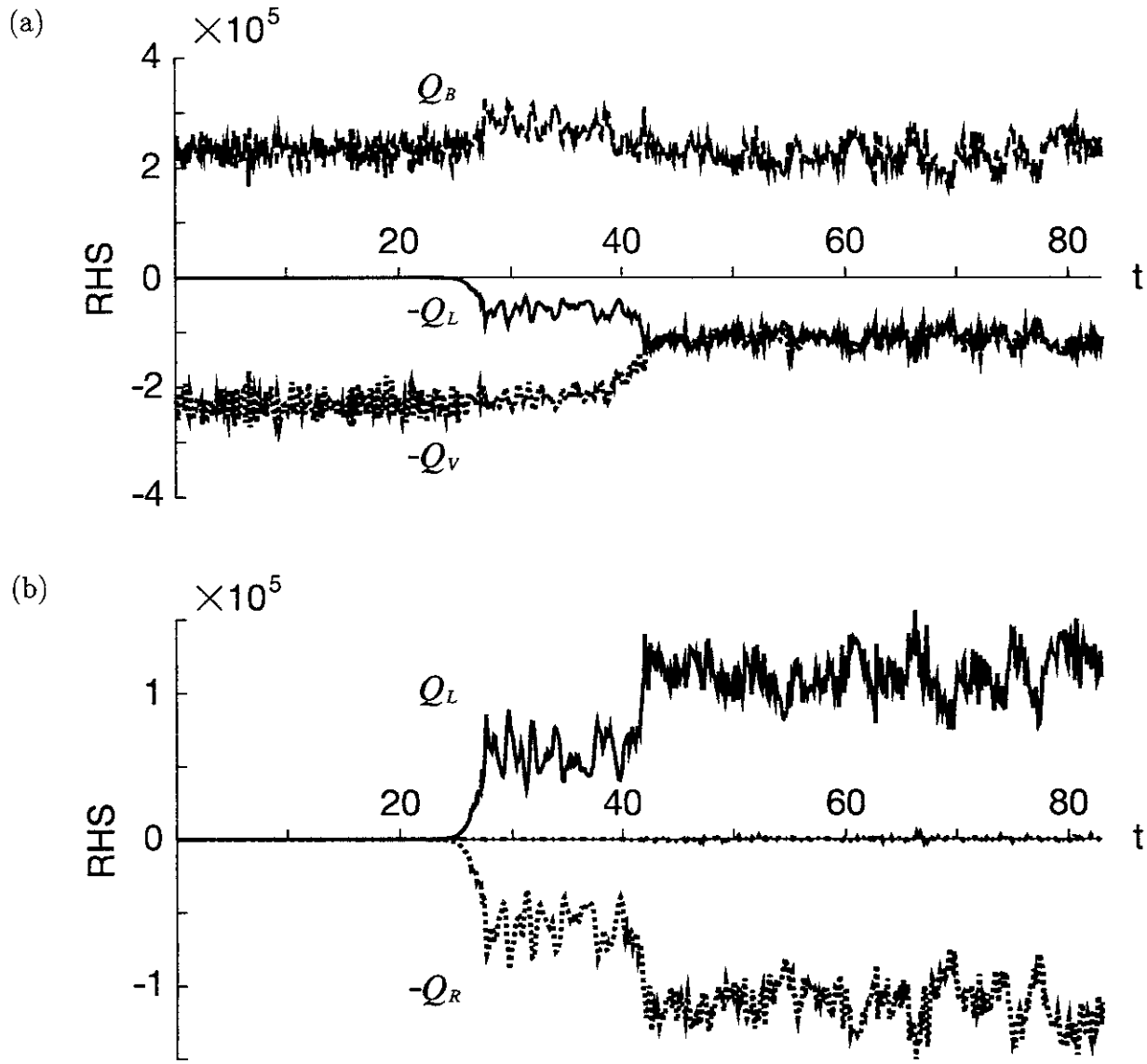

Figure 3: Contributions from the respective terms of the kinetic and magnetic energy equations. (a) Kinetic energy. $\mathcal{Q}_B$, buoyancy (– – –); $-\mathcal{Q}_L$, minus Lorentz (———); $-\mathcal{Q}_V$, minus viscous (· · · · ·). (b) Magnetic energy. $\mathcal{Q}_L$, Lorentz (———); $-\mathcal{Q}_R$, minus resistive (· · · · ·). A small fluctuating quantity seen on the abscissa denote the sum of the energy fluxes across the outer and inner boundaries.

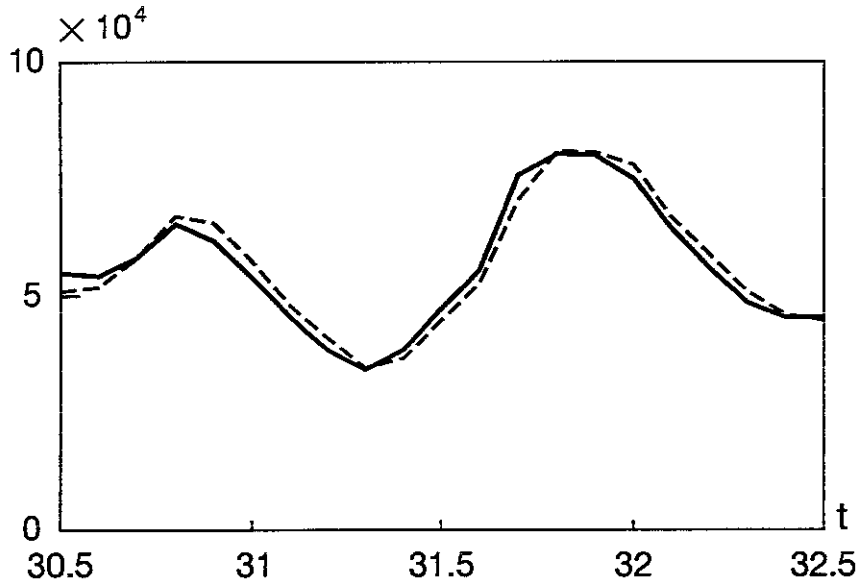

Figure 4: Phase lag between the stretching and resistive terms in the magnetic energy equation. Temporal variations of $\mathcal{Q}_L$ and $\mathcal{Q}_R$ are respectively plotted with a solid and a broken line during $30.5 \leq t \leq 32.5$, in the first-equilibrium period. The phase of variation of the former advances the latter by 0.03 time unit.

are very close, but the former always leads the latter by 0.03 time unit. This time lag, which is much smaller than any of the magnetic, viscous, and thermal diffusion times, should be interpreted as the magnetic energy transfer from large-to-small scales through nonlinear interactions. Incidentally, the very small fluctuations seen on the abscissa of figure 3(b) denotes the sum of the energy fluxes across the inner and outer boundaries.

Another interesting point to be mentioned is that as seen in figure 3(a), the contributions from the Lorentz and viscous forces are nearly equal in the second-equilibrium period. With reference to figure 3(b) this implies the equi-partition of energy dissipation between the velocity and magnetic fields.

Finally, a comment on the Colioris force term may be in order. Although it does not contribute to the energy budget at all, its effects on the velocity field should be significant in the present rapid rotating system. To confirm it, we calculated the root-mean-squares (RMS) of the respective terms on the right-hand side of Navier-Stokes equation (1) over the whole of the second-equilibrium periods. The relative ratios among them are stable (fluctuations being within 5% in the standard deviation) and their time averages are found to be

$$\text{(Pressure)} : \text{(Buoyancy)} : \text{(Colioris)} : \text{(Lorentz)} : \text{(Viscous)} = 2.0 : 1.6 : 1 : 0.7 : 0.2, \qquad (29)$$

which shows that the contribution from the Colioris term is quite large, as expected.

4.3 Magnetic Dipole Moment

One of the most important quantities in the problem of magnetic field intensification is the magnetic dipole moment defined by

$$\begin{aligned} \boldsymbol{m}(t) &= \int_{V_{\text{shell}}} \tfrac{1}{2}\boldsymbol{x} \times \boldsymbol{j}(\boldsymbol{x},t)\, \mathrm{d}V \\ &= \frac{3}{2}\int_{V_{\text{all}}} \boldsymbol{b}(\boldsymbol{x},t)\, \mathrm{d}V \left(\equiv \frac{3}{2}\lim_{R\to\infty}\int_{V_R} \boldsymbol{b}(\boldsymbol{x},t)\, \mathrm{d}V \right), \end{aligned} \tag{30}$$

where V_R denotes a sphere of radius R. The second identity is derived under the condition that the current density is confined in a finite domain as it is the case. Integral (30) is expressed in terms of the dipole ($l = 1$) component of the magnetic field in the spherical harmonic expansion. Let

$$\boldsymbol{b}(r,\theta,\phi,t) = \nabla \times A(r,\theta,\phi,t)\widehat{\boldsymbol{r}} + \nabla \times (\nabla \times B(r,\theta,\phi,t)\widehat{\boldsymbol{r}}) \tag{31}$$

be the toroidal and poloidal decomposition of the magnetic flux density in the spherical shell, where $A(r,\theta,\phi,t)$ and $B(r,\theta,\phi,t)$ are the toroidal and poloidal defining scalars, $\widehat{\boldsymbol{r}}$ is the unit radial vector, θ is the co-latitude, and ϕ is the longitude relative to the x axis. If the poloidal defining scalar is expanded in a series of the spherical harmonics as

$$B(r,\theta,\phi,t) = \sum_{l=0}^{N_\theta}\sum_{m=-l}^{l} B_{lm}(r,t)Y_{lm}(\theta,\phi), \tag{32}$$

then the three components of the magnetic dipole moment are written in terms of only the $l = 1$ components as

$$m_x(t) = 4\sqrt{3}\pi r_2\ \mathrm{Re}B_{11}(r_2,t), \tag{33}$$

$$m_y(t) = -4\sqrt{3}\pi r_2\ \mathrm{Im}B_{11}(r_2,t), \tag{34}$$

$$m_z(t) = 2\sqrt{6}\pi r_2\ B_{10}(r_2,t), \tag{35}$$

where Re and Im denote the real and imaginary parts, respectively.

The temporal evolution of the dipole moment is shown in figure 5. The magnitude is plotted in a semi-logarithmic scale in (a), the x, y, and z components are respectively represented by a solid, a dotted, and a dashed line in (b), and the angle between the dipole moment and the equatorial plane in (c). Here, the positive values imply that the dipole moment is pointed to the north. As seen in (a), the magnitude starts to increase exponentially in time and continues to grow throughout the first-equilibrium period until $t = 40$, then saturates around 800 in the second-equilibrium period. Very violent changes both in the amplitude and the direction of the dipole moment are observed in (a) and (c) around $t = 30$ which is the end of the linear period when the velocity and magnetic fields are about to adjust themselves to a new state. It is seen in (b) that among the three components, only the z component of the dipole moment changes in time substantially. It increases exponentially in time from the beginning until $t = 42$ when

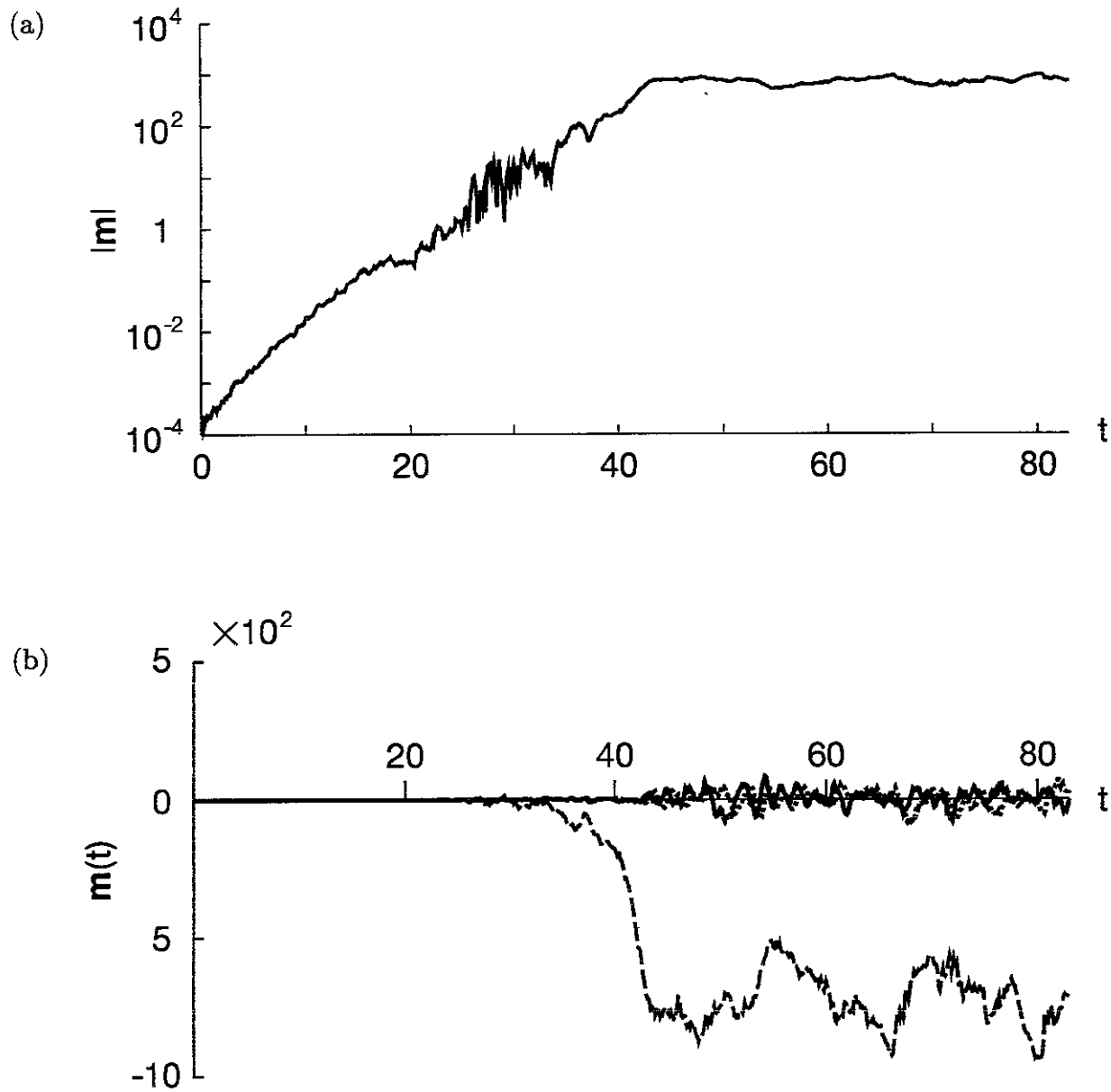

Figure 5: Temporal evolution of the magnetic dipole moment. (a) The magnitude $|\boldsymbol{m}|$ in a semi-logarithmic scale. It increases exponentially in time until $t = 42$, and then fluctuates around 800. Large fluctuations are observed around $t = 30$ which is the time when the linear period passes into the first-equilibrium period. (b) The x, y, z components. A solid, a dotted, and a dashed line refers to m_x, m_y, and m_z, respectively. After $t = 30$, the z component is dominant so that $|\boldsymbol{m}| \approx |m_z|$. (c) The angle between the dipole moment and the equatorial plane. Positive values indicate the northward direction.

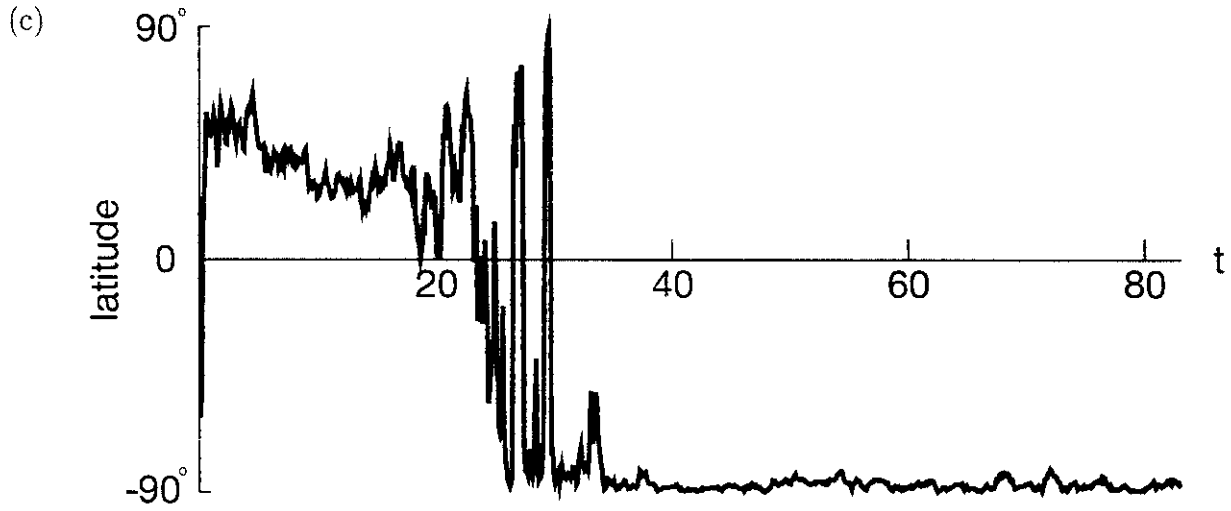

Figure 5(c) See page 18 for caption.

the system moves from the first- to the second-equilibrium periods. After $t = 30$, it becomes dominant and indistinguishable from the magnitude itself. The equatorial (x and y) components do not grow significantly so that the dipole moment is almost parallel to the rotation axis in the second-equilibrium period.[2] The variation of the z component in the second-equilibrium period is remarkably similar, apart from the sign, to that of the magnetic energy (cf. figure 2). This suggests that most of strong magnetic fluxes are pointed to the south. As seen in (c), the angle of the dipole moment measured from the equatorial plane is positive (i.e. pointed northward) in the linear period, which is accidental owing to the random initial condition. Later, in the first-equilibrium period, the dipole moment reverses a few times (Kida, Araki & Kitauchi 1997). Finally, in the second-equilibrium period, the direction is almost nailed to the south within 9^o deviation. This southward orientation of the magnetic field should have occurred also by chance. There is no indication of the change of sign of m_z, or reversal of the magnetic dipole polarity later in the second-equilibrium period. By comparing figures 2(a) and 5(a), we see that the magnetic energy and the magnetic dipole moment develop similarly but there is an interesting difference between the two. Both of them increase exponentially in time in the linear period and saturate in the second-equilibrium period. However, their behaviours in the first-equilibrium period are different from each other. The magnetic energy stays constant, whereas the dipole moment still increases exponentially in time with big fluctuations. In figure 6, we compare the temporal evolutions of the integration
over the equatorial plane of the square of b_z and the square of the integration of b_z. The temporal evolutions of these two are quite similar to those of the magnetic energy and the magnetic dipole moment, respectively (cf. figures 2(a) and 5(a)). This suggests that the activity of the magnetic field on the equatorial plane is a good representative of that in the whole space. As a matter of fact, except for the linear period, the activity of the magnetic

[2]Although the mean values of b_x and b_y are much smaller than that of b_z in magnitude, the RMS's of the former two are comparable with the latter.

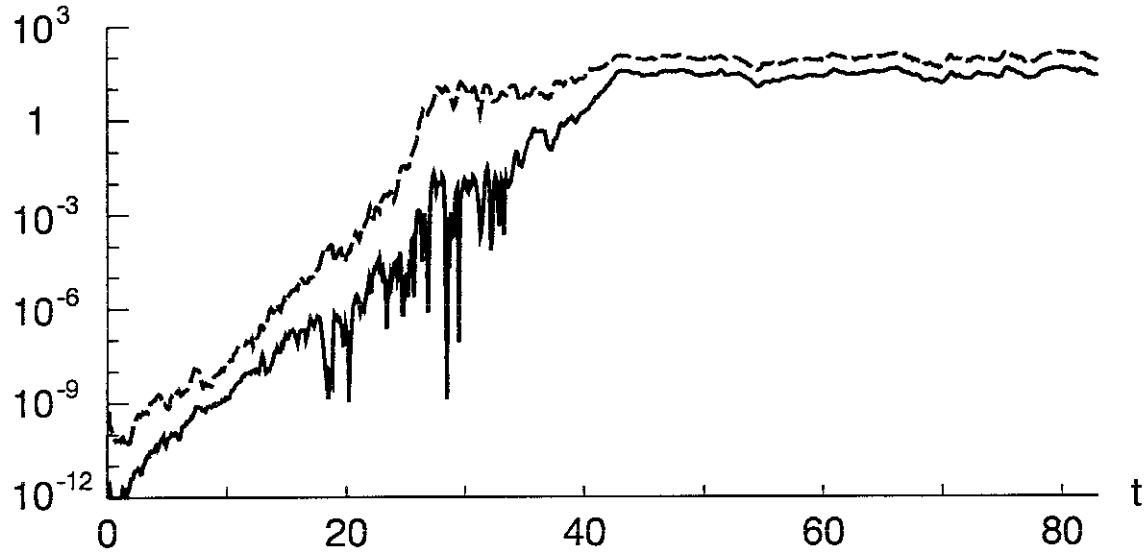

Figure 6: Temporal evolutions of two integral quantities of the magnetic field on the equatorial plane. The integration over the equatorial plane of the square of b_z and the square of the integration of b_z are plotted against time with broken and solid lines, respectively.

flux density, especially the z component, is maximal around the equatorial plane (see §5.3 and figure 15). We also find that the fluctuations of b_z are much larger than the mean value and that the former saturates at some level whereas the latter is still increasing in time in the first-equilibrium period. We speculate that the increasing arrangement (in anti-cyclones, see §5.1) of the direction of the magnetic field leads to the exponential growth of the mean value.

5 Stretch-and-Intensification of Magnetic Lines of Force

We have seen in §4 that there are three distinct periods in which the magnetic field develops differently. They are the linear, first-equilibrium, and second-equilibrium periods. The magnetic field is intensified in different ways in the respective periods, the physical characteristics in which are summarized in table 1. We consider the dynamo mechanism in each period separately in the following subsections.

5.1 Linear period

In the early stage of evolution the magnetic field is too weak to alter a thermal convection through the Lorentz force. Then, the magnetic field is passively intensified by a given velocity field. This period is therefore equivalent to the kinematic dynamo. Since the velocity field is hardly different from the pure thermal convection, the characteristics of the resulting magnetic field are almost the same throughout the linear period ($1 < t < 26$); namely, the mechanism of

Period	Linear	First-Equilibrium	Second-Equilibrium
Time	$1 < t < 26$	$28 < t < 38$	$t > 43$
Kinetic Energy	Stationary (= 2285)	Stationary (= 2239)	Stationary (= 1273)
Magnetic Energy	Exponential Growth	Stationary (= 4353)	Stationary (= 19626)
Vortex Columns	Alive	Broken	Broken
Number of ACs	9	9	$4 \sim 6$
Ang. Vel. of ACs	-0.90	-0.80	-0.8
Places of Intensification	$\langle a \rangle$, $\langle d \rangle$	$\langle a \rangle$, $\langle b \rangle$, $\langle c \rangle$, $\langle d \rangle$	$\langle b \rangle$, $\langle c \rangle$, $\langle d \rangle$

Table 1: Characteristics of the magnetic field in three periods of evolution. The magnetic energy is summed up over the whole space, whereas the kinetic energy in the spherical shell. AC implies the anti-cyclones. There are four particular places where the magnetic field is strongly intensified, i,e. $\langle a \rangle$ between a cyclone and its western neighbouring anti-cyclone off the equatorial plane, $\langle b \rangle$ inside anti-cyclones near the equatorial plane, $\langle c \rangle$ just outside of the Ekman boundary layer on the outer sphere near an anti-cyclone, and $\langle d \rangle$ between a cyclone and its western neighbouring anti-cyclone on the equatorial plane.

magnetic intensification may be understood by looking at the pure thermal convection velocity field. The intensity of the magnetic field, such as the magnetic energy and the dipole moment, increases exponentially in time. This continues until the Lorentz force becomes strong enough to deform the velocity field.

Snapshots of the vorticity and magnetic fields in the middle of the linear period are shown in figure 7. Iso-surfaces of $|\omega_z|$ with yellow for cyclones ($\omega_z > 0$) and blue for anti-cyclones ($\omega_z < 0$) are quite similar to those in the pure thermal convection (see figure 1). The lines on the equatorial plane represent the contours of ω_z with black for cyclones and white for anti-cyclones. The threshold on the contours is somewhat smaller than that on the iso-surfaces. Regions of high magnetic flux density are surrounded by red and pink iso-surfaces which indicate $b_z > 0$ and $b_z < 0$, respectively. This is viewed from 30° north latitude. Regions of strong magnetic field are observed in figure 7(a) between cyclones and their western neighbouring anti-cyclones in the middle latitude (between 29° and 61°) over almost all the radial coordinate ($0.06d < r - r_1 < 0.94d$). These are the places where the flow is accelerated away from the rotation axis (see figure 8 below). It is consistent with the results of Kitauchi & Kida (1998) that the magnetic field is intensified where the flow is pointed away from the rotation axis between cyclones and their western neighbouring anti-cyclones. In Kageyama & Sato (1997), on the contrary, the magnetic field intensification is observed at the places where the flow is pointed inward to the rotation axis. This discrepancy may be attributed to a subtle difference in the structure of the thermal convections owing to different values of control parameters. The magnetic field is anti-symmetric with respect to the equatorial plane. However, it seems of general characteristics in the present system that the magnetic field is intensified not equally between all the pairs of cyclones and their western neighbouring anti-cyclones but selectively between several of them (Kitauchi & Kida 1998), which is also different from the results in

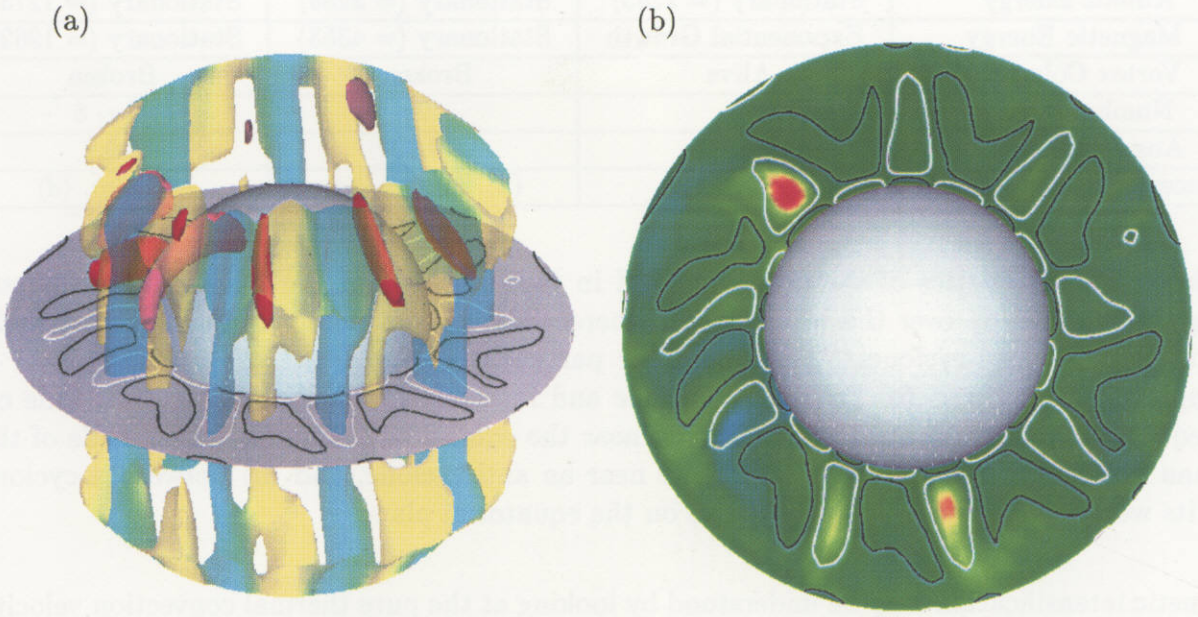

Figure 7: Snapshots of the vorticity and magnetic fields in the linear period. (a) Oblique views from 30^o north latitude. The iso-surfaces of the magnetic flux density $|\boldsymbol{b}|$ are drawn with red for $b_z > 0$ and pink for $b_z < 0$, inside of which it takes larger values in magnitude. Iso-surfaces of $|\omega_z|$ are drawn with yellow for cyclones ($\omega_z > 0$) and blue for anti-cyclones ($\omega_z < 0$). Contours of ω_z are drawn on the equatorial plane at a somewhat lower level in magnitude. The black lines are for cyclones and the white for anti-cyclones. (b) A cross-section of the fields on the equatorial plane viewed from the north. The magnetic flux density is shown with colour map in which red is for positive flux and blue is for negative. The magnetic field is intensified between cyclones and their western neighbouring anti-cyclones in the middle latitude and inside anti-cyclones on the equatorial plane. $t = 15$.

Kageyama & Sato (1997). By comparing the iso-surfaces of the magnetic flux density at successive times (not shown here), we find that the pattern of strong magnetic regions prograde relative to the convection vortices. In the meantime, as seen in figure 7(b), the magnetic field is being intensified inside of anti-cyclones on the equatorial plane. This activity is much weaker than that in the middle latitude at this time, but it becomes more important later in the first- and second-equilibrium periods (see §§5.2 and 5.3).

The regions of strong magnetic field shown in figure 7 are understood by comparing it with the velocity field. In figure 8, we plot the velocity and magnetic fields at time $t = 15$ on a sphere of radius $r = r_1 + 0.55d$ where the magnetic field is strongest. They are viewed from 30^o north latitude. Red-white lines with a black dot represent the streamlines projected on the sphere in a frame moving with the convection vortices. The flow is toward the dot with accelerating on red and decelerating on white. The radial component u_r of velocity is generally smaller than the azimuthal components, which is shown by colour map with blue for positive

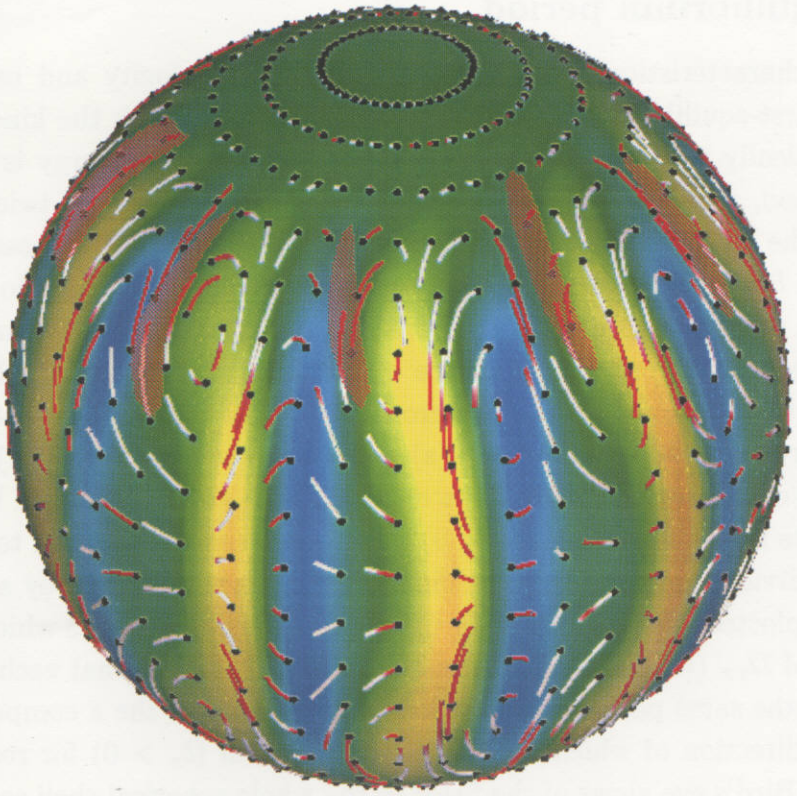

Figure 8: Stretching of magnetic lines of force between cyclones and anti-cyclones in the linear period. The streamlines projected on a surface of radius $r = r_1 + 0.55d$ are drawn with red-white lines with a black dot. The flow is pointed toward the dot. The acceleration is positive on the red part and negative on the white. The velocity field is seen in a frame moving with the convection vortices. The radial component of velocity is much smaller than the azimuthal components. The brown iso-surfaces represent regions of high magnetic flux density. The magnetic field is intensified in accelerating regions. An oblique view from 30^o north latitude at $t = 15$.

and yellow for negative. The strong magnetic field is observed at accelerating regions where the magnetic lines of force are being stretched.

There is another intensified region, classified as $\langle d \rangle$ in table 1, between cyclones and their western neighbouring anti-cyclones on the inner-sphere side at low latitude. It happens to be invisible in figure 7 because this region is rather narrow and the magnetic field there is a bit weaker than that in $\langle a \rangle$. However, we have confirmed its existence at other times (cf. figure 16 in §5.4) and identified it with the one discovered before by Kitauchi & Kida (1998).

The magnetic field which has been intensified by the above mechanism deforms the velocity field through the Lorentz force to stop the growth of the magnetic field itself, and we enter the

first-equilibrium period during which the magnetic energy is statistically stationary.

5.2 First-equilibrium period

Two prominent characteristics in the development of the velocity and magnetic fields are observed in the first-equilibrium period ($28 < t < 38$). First, both the kinetic and magnetic energy are statistically stationary. The level of the mean kinetic energy is the same as that in the linear period, whereas the magnetic energy is increased to be twice as large as the kinetic. Second, the magnitude of the magnetic dipole moment is still increasing exponentially in time (see figure 5(a)). We describe in this section the structure of the velocity and magnetic fields in detail. In order to capture the temporal behaviour of the velocity and magnetic fields we show, in figure 9, a typical time sequence of the fields in this period. The green circular annulus denotes the equatorial plane. The cross-sections of the fields on the equatorial plane seen from the north are shown in figure 9(a). The time elapses from (a-i) to (a-xii) by 0.3 time unit. The z component of vorticity is depicted with contour lines of black for cyclones ($\omega_z > 0$) and white for anti-cyclones ($\omega_z < 0$). The magnitude is common to the both lines at all times. The individual anti-cyclones at different times are identified by attached numbers. These figures are plotted in a frame moving with the convection vortices which retrograde with angular velocity of Ω_{TP} ($= -0.8$) relative to the spherical shell so that each vortex is located approximately at the same position. The colour map represents the z component of magnetic flux density, the direction of which is pointed to the north ($b_z > 0$) for red or to the south ($b_z < 0$) for blue. Bird's eye views of the fields in the whole spherical shell seen from 30^o north latitude are pictured in figure 9(b), in which red surfaces represent the magnitude of magnetic flux density and gray semi-transparent ones the vorticity magnitude.

It is seen in figure 9(a) that all the nine cyclones and anti-cyclones, which were born in the linear period, are robust and not destroyed though their shapes are much deformed. Actually they survive and the individual vortices can be traced unambiguously throughout the first-equilibrium period. The most remarkable observation on the equatorial plane is that [1] the strong magnetic flux is confined only in the anti-cyclones, [2] they do not occupy all the anti-cyclones but only in several of them, [3] the intensity of the magnetic flux density in each anti-cyclone varies in time; some changes the sign and others do not before and after a vanishing intensity, and [4] the shape of vorticity contours is different depending on the magnitude of magnetic field in them; the stronger is the magnetic field, the rounder the shape.

Point [3] may need an explanation. Slightly yellow anti-cyclone #4 in (a-i) changes into blue. It becomes brightest in (a-iv), then fades away in (a-vi). Thereafter, it gets yellow and red, then blue again in (a-x) and goes on. Thus, it changes the sign alternately. The same behaviour is clearly observed in five other anti-cyclones #1, #3, #5, #7, and #8. The way of change of sign in anti-cyclones #2 and #6 is similar though the intensity is rather weak. On the other hand, vortex #9 in (a-i) gets weaker and disappears around (a-iv)$\sim$(a-v), but reappears as the same colour, gets stronger in (a-vii), then weaker again and disappears around (a-xi)$\sim$(a-xii).

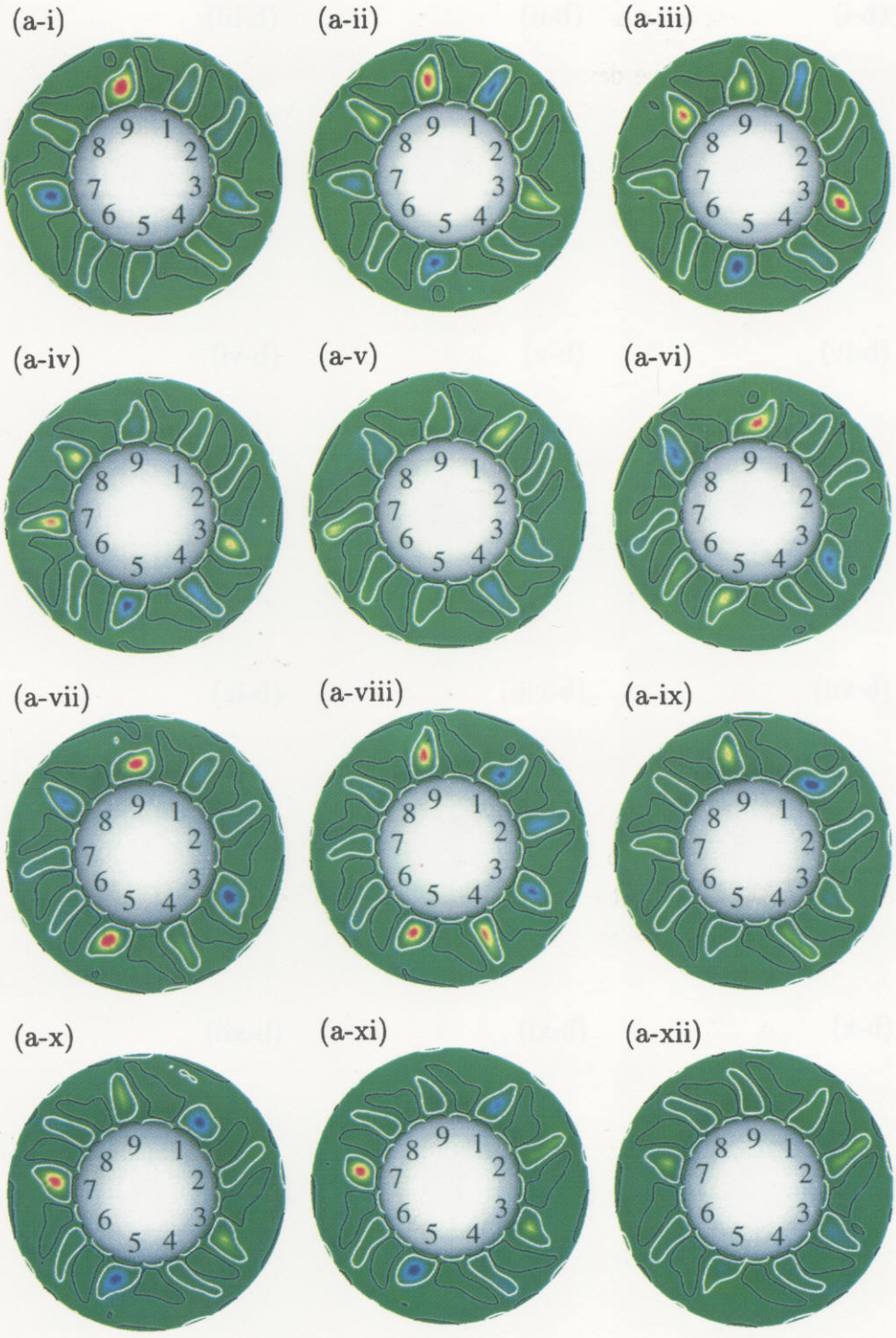

Figure 9(a): See page 27 for caption.

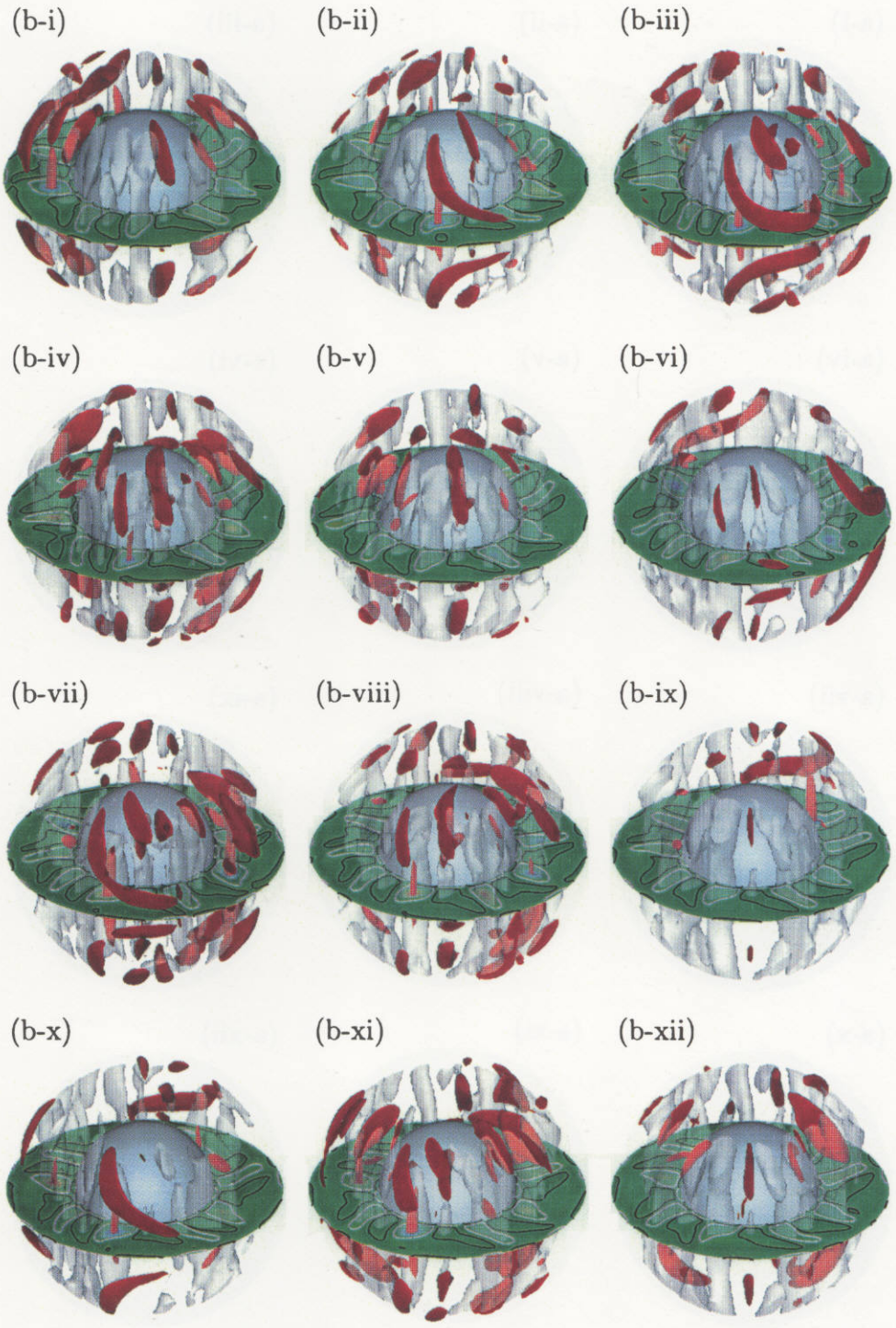

Figure 9(b). See page 27 for caption.

Indeed the behaviour on the equatorial plane is simpler in appearance, but the dynamics of the system cannot be closed on this plane. The spatial distribution of iso-surfaces of $|\boldsymbol{b}|$ in figure 9(b) shows that the magnetic flux is more intense off the equatorial plane. Their temporal variations are rather complicated, but a careful inspection enables us to extract dynamically important blobs of intense magnetic field and to classify them into four groups, i.e.

$\langle a \rangle$ cigar-shaped ones generated at middle latitude between a cyclone and its western neighbouring anti-cyclone,

$\langle b \rangle$ cigar-shaped ones penetrating orthogonally the equatorial plane at the center of anti-cyclones,

$\langle c \rangle$ banana-shaped ones associated with $\langle b \rangle$ which are located between anti-cyclones and the outer boundary,

$\langle d \rangle$ horn-shaped ones generated at low latitude on the inner-sphere side between a cyclone and its western neighbouring anti-cyclone.

The first type $\langle a \rangle$ has already appeared in the linear period. The appearance of the fourth type $\langle a \rangle$ is very rare (cf. light-blue dots in figure 16 of §5.4).

One of the most interesting observations discovered in the bird's-eye view is that the types $\langle b \rangle$ and $\langle c \rangle$ always appear together with. In order to see the way of their appearance more closely we trace the field in detail in figure 10 which is an enlargement of a period around figure 9(b-vii). First, look at a yellow anti-cyclone (the one numbered 5 in figure 9(a)) at the bottom left. There is nothing with it in (i). A banana-type blob begins to appear in (ii) and develops subsequently. Then, in (iv), a vertical cigar-type blob appears in an associated anti-cyclone. It develops and gets strongest in (vi), then weakens and disappears in (ix). The same process occurs with a blue anti-cyclone (#3 in figure 9(a)) at the right and with a yellow anti-cyclone (#9 in figure 9(a)) at the top. A banana-type blob exists already in each of these anti-cyclones in (i). Then, in the following panels, vertical cigar-type blobs appear in the respective anti-cyclones, which develop strongest in (v) and then fade away approximately at the same time.

Figure 9: Temporal evolutions of the magnetic and velocity fields in the first-equilibrium period. (a) Equatorial plane seen from the north. Contour lines of ω_z are drawn with black for positive vorticity (cyclones) and white for negative (anti-cyclones). The magnitude of vorticity is the same on all lines at all times. The numbers identify the individual anti-cyclones at different times. The colour map on the plane represents b_z. Red is for positive flux, blue is for negative, and green is for zero. (b) Bird's-eye views of the magnetic field seen from 30° north latitude. The red surfaces represent $|\boldsymbol{b}|$ and the gray semi-transparent ones $|\boldsymbol{\omega}|$. The levels of these iso-surfaces are common at all times. (i) $t = 28.0$, (ii) 28.3, (iii) 28.6, (iv) 28.9, (v) 29.2, (vi) 29.5, (vii) 29.8, (viii) 30.1, (ix) 30.4, (x) 30.7, (xi) 31.0 (xii) 31.3.

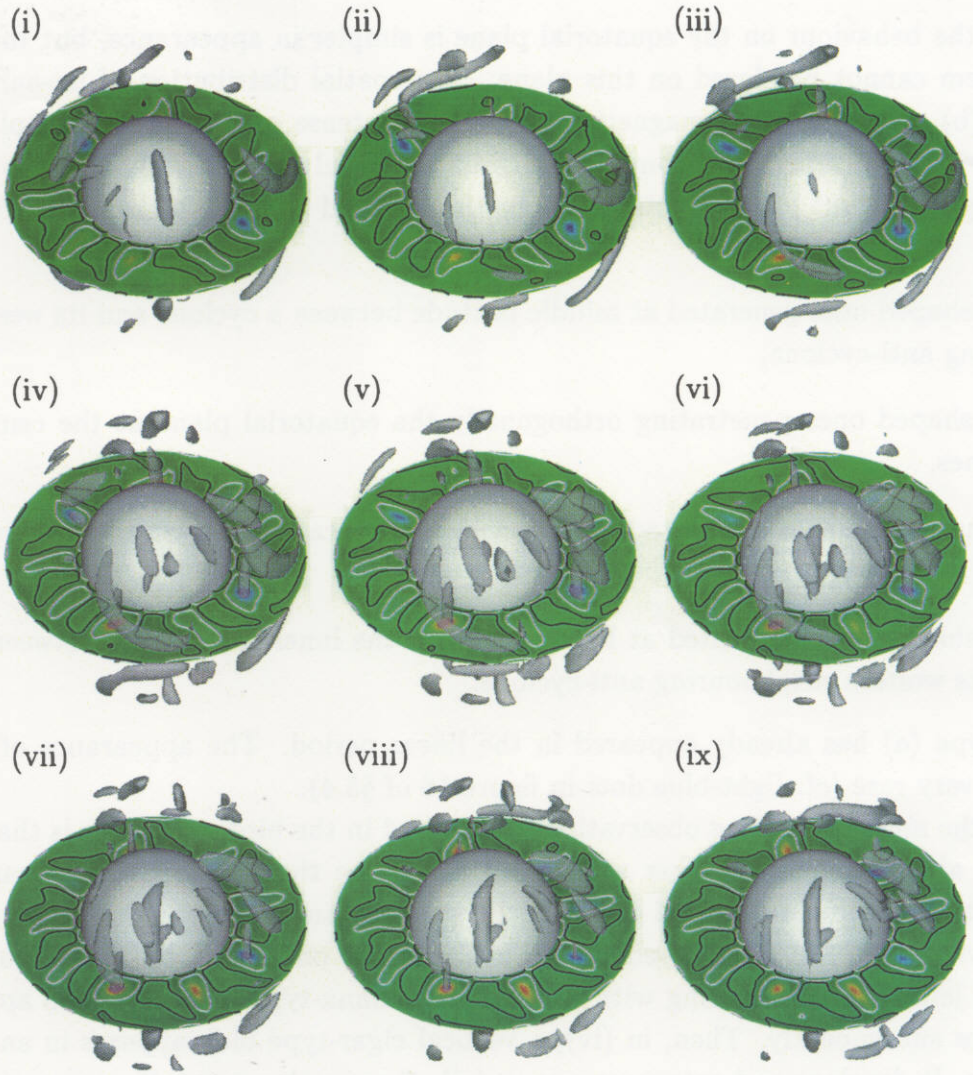

Figure 10: Simultaneous appearance of cigar-shaped and banana-shaped blobs of high-magnetic flux density. The gray iso-surfaces represent $|\boldsymbol{b}|$. The fields on the equatorial plane is plotted in the same manner as figure 9(a). (i) $t = 29.4$, (ii) 29.5, (iii) 29.6, (iv) 29.7, (v) 29.8, (vi) 29.9, (vii) 30.0, (viii) 30.1, (ix) 30.2.

The directions of magnetic fluxes of these blobs are perfectly correlated to each other. In order to see the connection between the two blobs directly we show in figure 11 the magnetic lines of force which go through inside an anti-cyclone at $t = 29.8$. It is seen that these lines actually run along the banana-shaped blob. By the way, the symmetry of the magnetic field with respect to the equatorial plane is still well maintained.

The formation mechanism of the banana-shaped blobs of the strong magnetic field may be seen in figure 12, where the magnetic and velocity fields on a surface of radius $r = r_1 + 0.92d$ just outside of the Ekman boundary layer are depicted. Streamlines projected on the sphere are drawn with red-white lines with black circles. The flow is directed toward the circles while

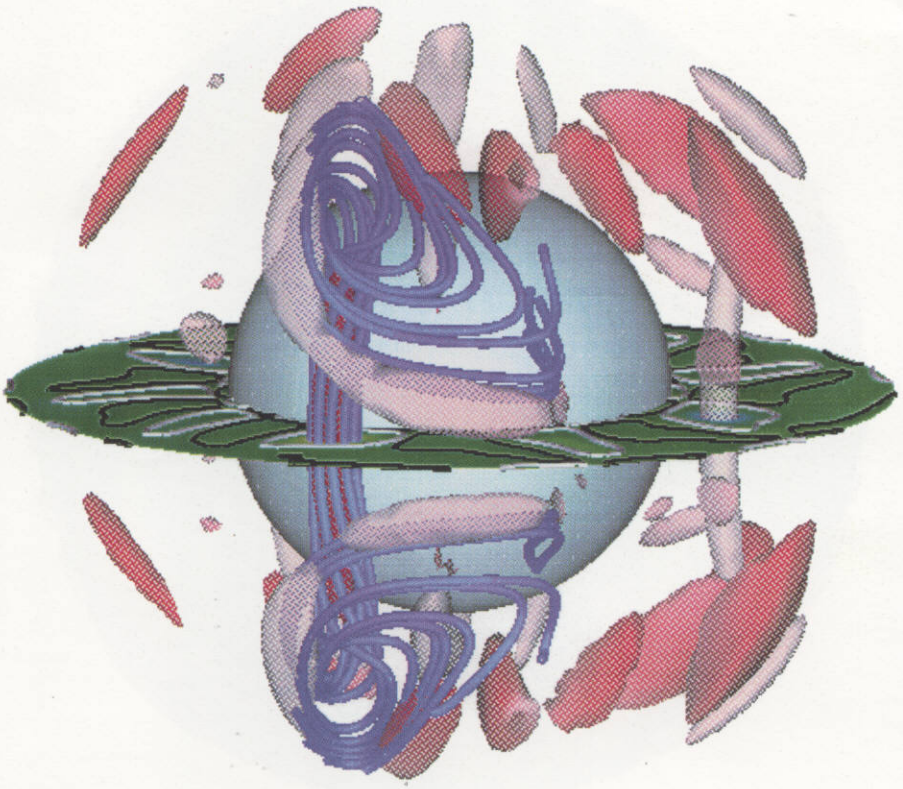

Figure 11: Connection between a cigar-shaped strong magnetic blob in an anti-cyclone and a banana-shaped one outside. Magnetic flux lines which go through a circle of radius $0.1d$ located at the center of an anti-cyclone (which is #5 in figure 9(a)) are drawn with purple lines. The coloured surfaces represent the iso-surfaces of $|\boldsymbol{b}|$ with red for $b_z > 0$ and pink for $b_z < 0$. $t = 29.8$.

accelerated on red and decelerated on white. The colour map denotes the radial component of velocity with blue for positive and yellow for negative. The white cross indicates the stagnation point, from which the convection flow extends with positive acceleration both toward the south-east and the north-west and the intensified magnetic field shown with brown iso-surfaces is created through stretching of magnetic lines of force.

It is interesting to compare the shape of the magnetic lines of force shown in figure 11 with the ones discussed by Olsen, Christensen & Glatzmaier (1999) as the mutual generation mechanism of the toroidal and poloidal fields (see figures 5 and 8 in their paper). They show a similar 'twist-turn' loop of the magnetic lines of force which penetrates orthogonally the equatorial plane and are twisted at a higher latitude toward the outer sphere, to the east, and to lower latitudes. Indeed the shape of the field lines are quite similar, but their explanation of the generation mechanism is rather different from ours. They explain it, similarly to Kageyama & Sato (1997), by the inward fluid motion between a pair of convective vortices (a cyclone being in the west and an anti-cyclone in the east) and the axial flows which are directed away from the equatorial plane in the cyclone and toward the equatorial plane in the anti-cyclone.

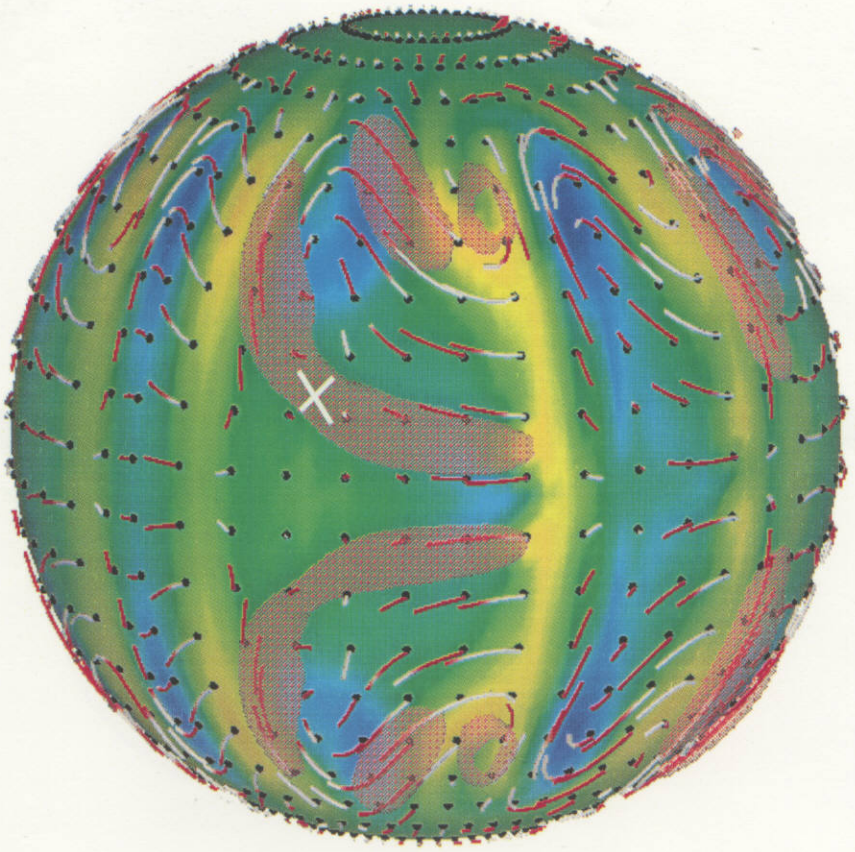

Figure 12: Stretch-and-intensification of magnetic lines of force near the outer sphere. Streamlines projected on a sphere of radius $r = r_1 + 0.92d$ are drawn with red-white lines with black dots, where r_1 is the inner-sphere radius and d the shell thickness. The flow, which is pointed toward the dots, is accelerating on red and decelerating on white. The colour map represents the radial component of velocity with blue for positive and yellow for negative. The magnetic flux density is stronger in the semi-transparent brown iso-surfaces. A stagnation point of the projected streamlines is indicated with white $\times$. The magnetic field is intensified on accelerating streamlines. $t = 29.8$

As a result, the magnetic field is intensified outside the convection vortices. In contrast, we have observed that it is intensified inside of anti-cyclones and on their outer-boundary side by the concentrate-and-stretch mechanism.

5.3 Second-equilibrium period

The interaction between the velocity and magnetic fields is much complicated in the second-equilibrium period ($t > 43$). The magnetic energy is 15 times as large as the kinetic energy so that the velocity field is much distorted from the pure thermal convection state. A developed magnetic field destroys the quasi-two-dimensional vortex columns along the rotation axis. On the other hand, the imposed temperature difference between the inner and outer spheres always

works to generate new convection vortices. As a result, some numbers of vortices remain in the field all the time. The dipole component of the magnetic flux density is dominant in this period, and the magnetic field exhibits a typical dipole structure in vacuum outside of the spherical shell (See figure 2 in Ishihara & Kida 2000). The axis of the dipole field is aligned with the rotation axis, so that this is called the axial magnetic dipole field.

As seen in figure 2, the magnetic energy fluctuates in time with quite large amplitude in the second-equilibrium period. It exhibits a sawtooth oscillation with period of about 15 d^2/ν (which is comparable with the magnetic diffusion time $d^2/\lambda = 10\ d^2/\nu$). In order to see typical temporal evolutions of the velocity and magnetic fields we pick up a single time period between the first and second big minima ($54.7 < t < 66.3$). Figures 13 and 14 show their evolutions in the growing phase ($t = 54.2 \sim 64.1$) and the decaying phase ($t = 65.9 \sim 70.7$), respectively. The representation is the same as in figure 9. Only a single level of $|\omega_z|$ is plotted on the equatorial plane so that a double contour of an anti-cyclone indicates the existence of a hollow at the center. The colour represents b_z with blue for negative, green for zero, and yellow for positive. Note that it is negative in all the anti-cyclones.

Several interesting characteristic features are observed in these figures. First, let us look at the vorticity field in each snapshot. [1] The white contours are much wider than the black, meaning that anti-cyclones are much stronger than cyclones (see figures 13(a) and 14(a)). This is a contrast to the linear and first-equilibrium periods in which the two kinds of vortices are more or less the same in strength. [2] The number of anti-cyclones is not invariant in time but varies between 4 and 6. They tend to arrange themselves with equi-distance apart from each other around the equatorial annulus (for example, see figure 14(a-iv) for the four-vortex state, figures 13(a-i), 13(a-iii) and 14(a-viii) for the five-vortex state, and figures 13(a-xii) and 14(a-ii) for the six-vortex state. Recall that there were nine pairs of cyclones and anti-cyclones both in the linear and first-equilibrium periods. This implies that a vortex break-down should have occurred just before entering the second-equilibrium period. [3] There are quite a few doubly-contoured anti-cyclones most of the time. These are hollow vortices, namely, vorticity is lower at the center. (N.B. All the contours have the same level of vorticity.) [4] Anti-cyclones are localized in the vicinity of the equatorial plane as opposed to the columns elongated along the rotation axis observed in the linear and first-equilibrium periods (see figures 13(b) and 14(b)). It is clearly seen in the bird's-eye views that the regions of intensified magnetic field are also different from the preceding periods. Cigar-shaped regions (classified as $\langle b \rangle$) penetrating vertically the equatorial plane at the centers of the anti-cyclones are prominent. They are much stronger inside of hollow vortices (see, for example, #1 in figures 13(b-x), 13(b-xii) and 14(b-i), #2 in 13(b-ii) and 13(b-viii), #3 in 13(b-ix), #5 in 13(b-v), 13(b-xii) and 14(b-i)-(b-iii), #6 in 13(b-vii), #7 in 13(b-10), 13(b-xii), and 14(b-ix)). Banana-shaped regions (classified as $\langle c \rangle$) along the outer sphere appear accompanied with the above cigars.

On the other hand, other cigar-shaped regions (classified as $\langle a \rangle$) between cyclones and their western-neighbouring anti-cyclones, which were observed in the linear and first-equilibrium periods, have disappeared. Horn-shaped regions (classified as $\langle d \rangle$) are now seen at the east side of some anti-cyclones on the equatorial plane in 13(b-iii), (b-ix)-(b-xi) and 14(b-iii), (b-v),

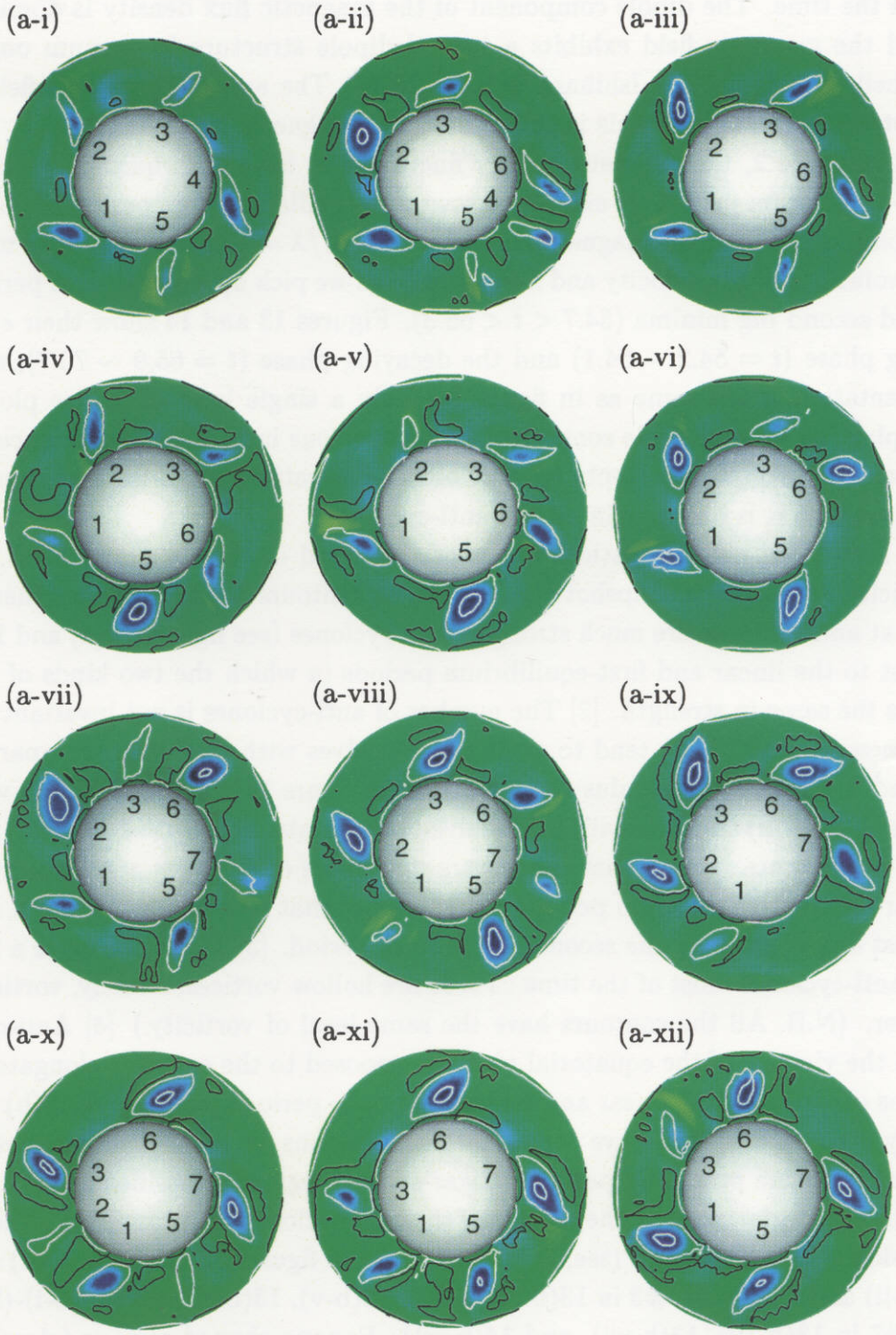

Figure 13(a): See page 33 for caption.

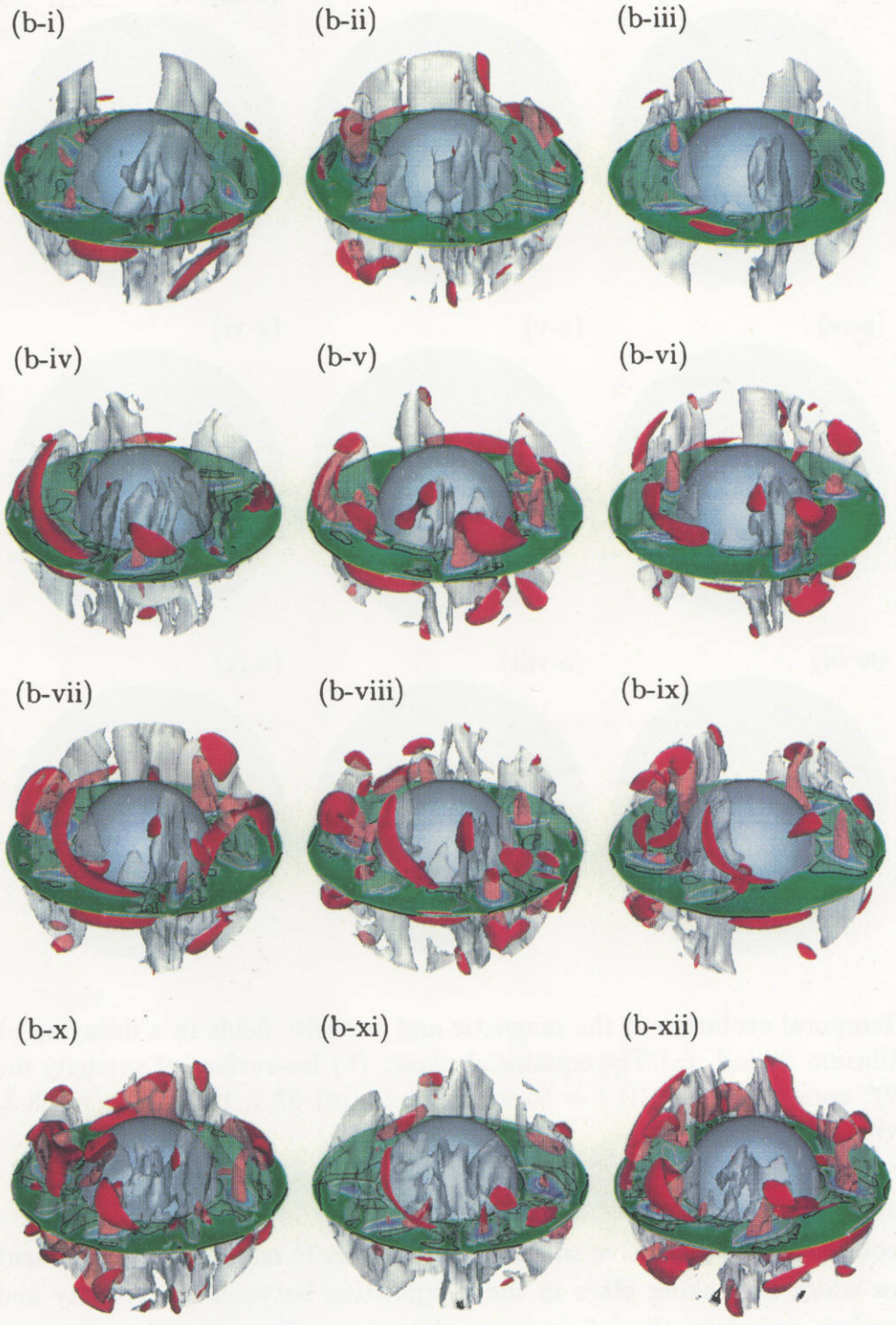

Figure 13: Temporal evolutions of the magnetic and vorticity fields in a growing phase of the second-equilibrium period. (a) The equatorial plane. (b) Oblique views from 30^o north latitude. The red iso-surfaces represent $|\boldsymbol{b}|$ and the gray semi-transparent ones $|\boldsymbol{\omega}|$. (i) $t = 54.2$, (ii) 55.1, (iii) 56.0, (iv) 56.9, (v) 57.8, (vi) 58.7, (vii) 59.6, (viii) 60.5, (ix) 61.4, (x) 62.3, (xi) 63.2, (xii) 64.1.

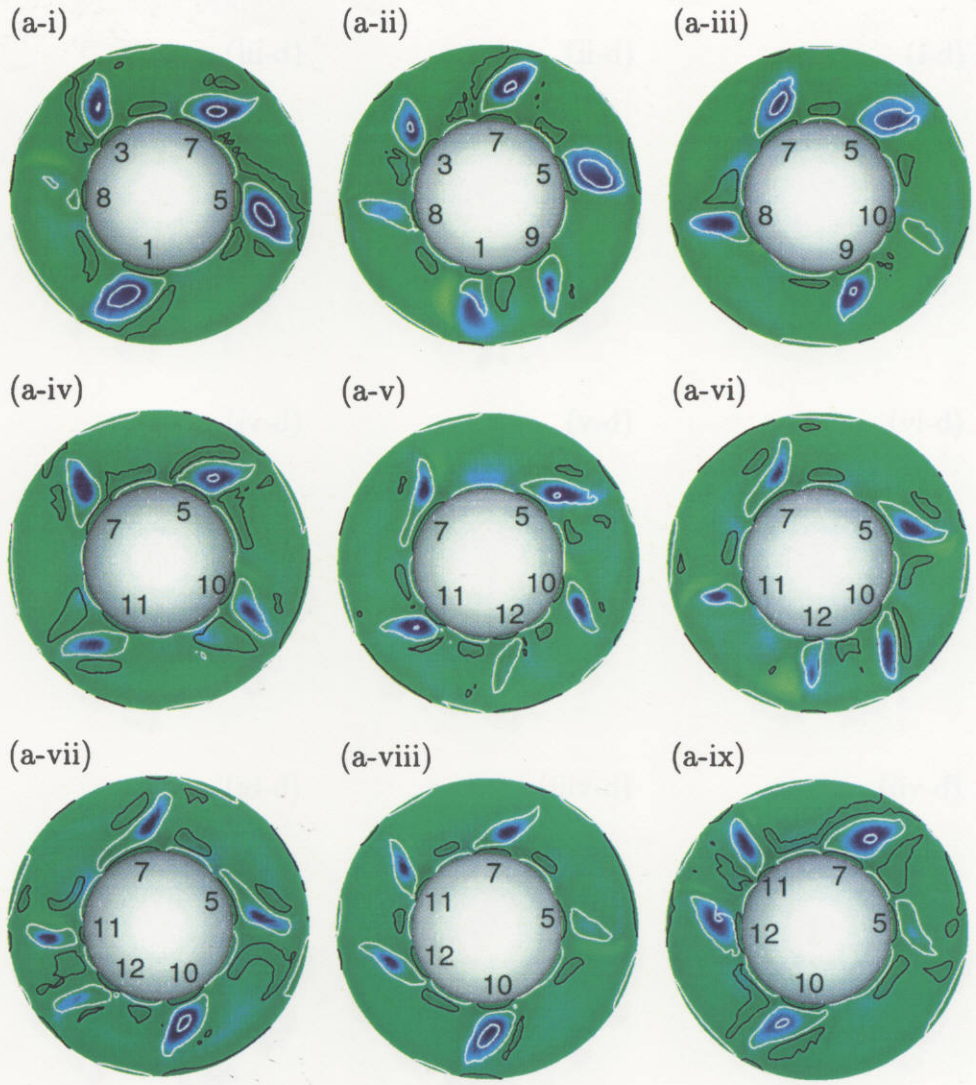

Figure 14: Temporal evolution of the magnetic and vorticity fields in a decaying phase of the second-equilibrium period. (a) The equatorial plane. (b) Iso-surface of vorticity magnitude A view from 30^o north latitude. (i) $t = 65.9$, (ii) 66.5, (iii) 67.1, (iv) 67.7, (v) 68.3, (vi) 68.9, (vii) 69.5, (viii) 70.1, (ix) 70.7.

(b-vi), (b-viii), (b-ix).

Next, a comparison of successive snapshots enables us to educe some fundamental dynamical processes which are taking place in the competition between the velocity and magnetic fields. Remember, as before, these figures are plotted in a frame rotating with mean angular velocity -0.8 of the vorticity pattern so that we can identify the individual vortices. (Note, however, that the position of vortices moves to and fro considerably because the flow motion is much more violent and the instantaneous angular velocity fluctuates quite a large around the mean value.) By tracing the individual anti-cyclones carefully, we find that they have a common life cycle. As stated before, the number of anti-cyclones changes in time between 4 and 6, which implies that they have finite life-times. Just after an anti-cyclone has disappeared,

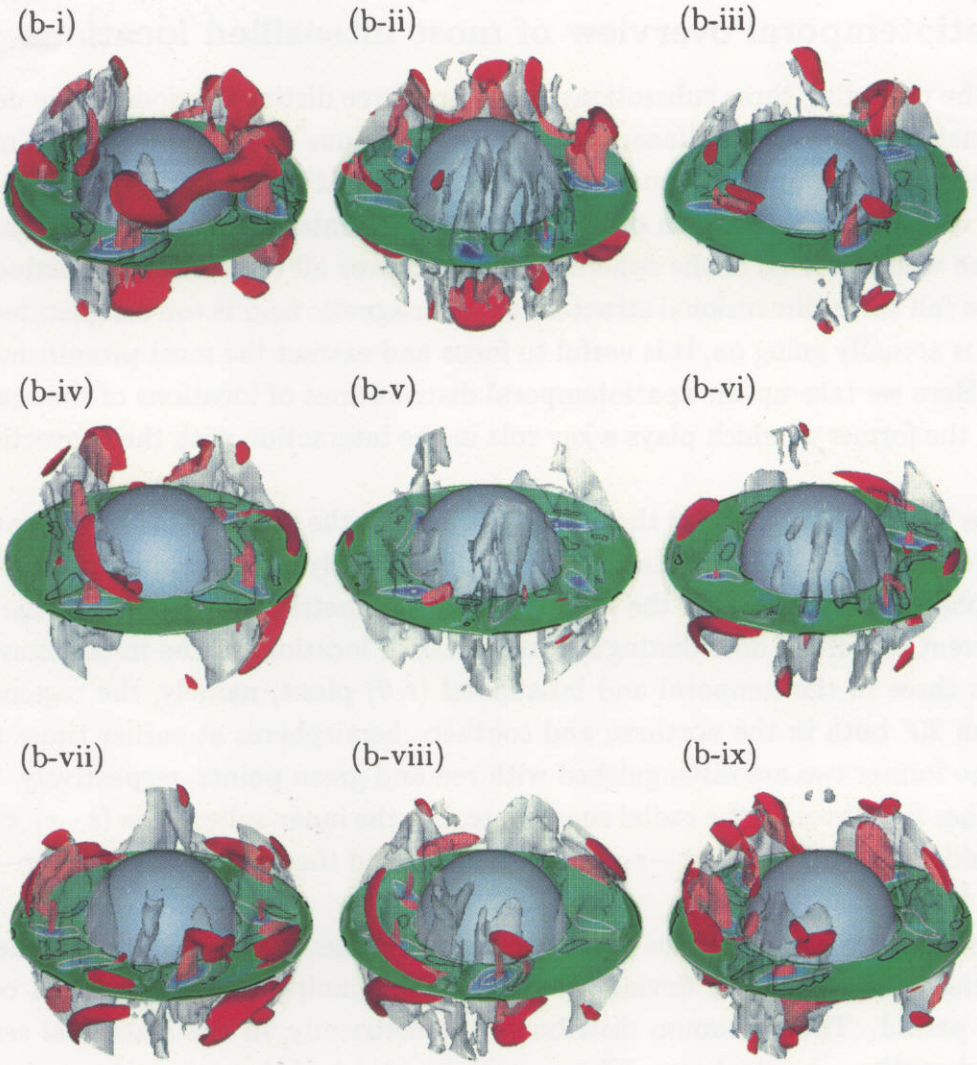

Figure 14(b): See page 34 for caption.

there remain weak fluctuations of vorticity at the place where it was. After a while, a new anti-cyclone is born somewhere around the above place. It develops with increasing vorticity. At the same time magnetic flux density is being intensified inside of this anti-cyclone. In the meanwhile the vorticity contours (of the same level) get doubled, meaning the appearance of a vorticity hollow at the center. Thereafter such a double contour shows a little complex behaviour. It weakens to a single contour, returns to a double once again, then weakens to a single, and finally disappears completely.

Let us trace some of typical vortices which exhibit (a part of) the above life cycle of anti-cylones. Anti-cyclone #6 is born in 13(a-ii) between those of #3 and #4. It is gradually intensified to grow up to a hollow vortex in 13(a-vi). Then, it keeps its shape for some time and disappears between 13(a-xii) and 14(a-i). Similar behaviours are observed for other vortices except for #4 and #8. This life cycle of anti-cyclones will be discussed in more detail in §6.

5.4 Spatiotemporal overview of most intensified locations

As seen in the preceding three subsections, there are three distinct periods in the development of the magnetic field, i.e. the linear, and first-equilibrium and second-equilibrium periods. The mechanism and the place of magnetic field intensification are different in the respective periods. In this section we take an overview of the most intensified locations of the magnetic field over the whole volume of the spherical shell and over all the simulation period.

Since the full three-dimensional structure of the magnetic field is too complicated to understand what is actually going on, it is useful to focus and extract the most prominent characteristics of it. Here we take up the spatiotemporal distributions of locations of the maximums of $|b_z|$ and $|b|$, the former of which plays a key role in the interaction with the convection velocity field.

In figures 15 and 16, we plot (a) the latitudinal and (b) the radial positions of the maximums of $|b_z|$ and $|b|$ over the whole simulation period, respectively. The maximums are searched in each hemisphere separately since the field is nearly symmetric with respect to the equatorial plane. Different colours of dots distinguish the areas of locations of the maximums. They are divided into three in the temporal and latitudinal (t, θ) plane, namely, the regions of higher latitude than 20^o both in the northern and southern hemispheres at earlier times $t < 40$ and the rest. The former two are distinguished with red and green points, respectively. The rest is divided further into three by the radial coordinate, i.e. the inner-sphere side ($r - r_1 < 0.3d$, light blue), the middle region ($0.3d < r - r_1 < 0.7d$, yellow) and the outer-sphere side ($r - r_1 > 0.7d$, dark blue). [3]

It is seen in figure 15(a) that the maximums are localized at the middle latitude ($37^o \pm 6^o$, where $\pm$ denotes the standard deviation) from the beginning through the end of the first-equilibrium period. The maximum distributes symmetrically, in the statistical sense, in the northern and southern hemispheres. These are the part $\langle a \rangle$ of the strong magnetic field intensified between cyclones and their western neighbouring anti-cyclones (see table 1 and figure 7). Their radial position is scattered over the outer half ($0.26d < r - r_1 < 0.94d$) of the spherical shell (figure 15(b)). Around $t = 28$, the beginning of the first-equilibrium period, new maximums, shown with yellow dots, appear around the middle radial region on the equatorial plane. They are localized in a narrow annulus at $0.26d < r - r_1 < 0.40d$ throughout the first-equilibrium period ($28 < t < 38$). This is nothing but the central region of anti-cyclones at which the magnetic field is intensified through stretching of magnetic lines of force perpendicularly to the equatorial plane, which is classified as $\langle b \rangle$ in Table 1. The maximums of the part $\langle a \rangle$ are still observed at the same place. Coexistence of $\langle a \rangle$ and $\langle b \rangle$ are the characteristics of the first-equilibrium period (see below for the third one $\langle c \rangle$).

Later, in the second-equilibrium period ($t > 43$) these maximum positions of $\langle b \rangle$ spread out more in both the latitudinal and radial directions, which is the manifestation of more violent activity of the magnetic field. The red and green dots (maximums classified as $\langle a \rangle$) disappear

[3] There are a few exceptional points which are categorized wrongly by this formal criterion. For example, the lowest red on at the initial time is located just below 20^o latitude (see figure 15(a)). These points are classified appropriately by hand.

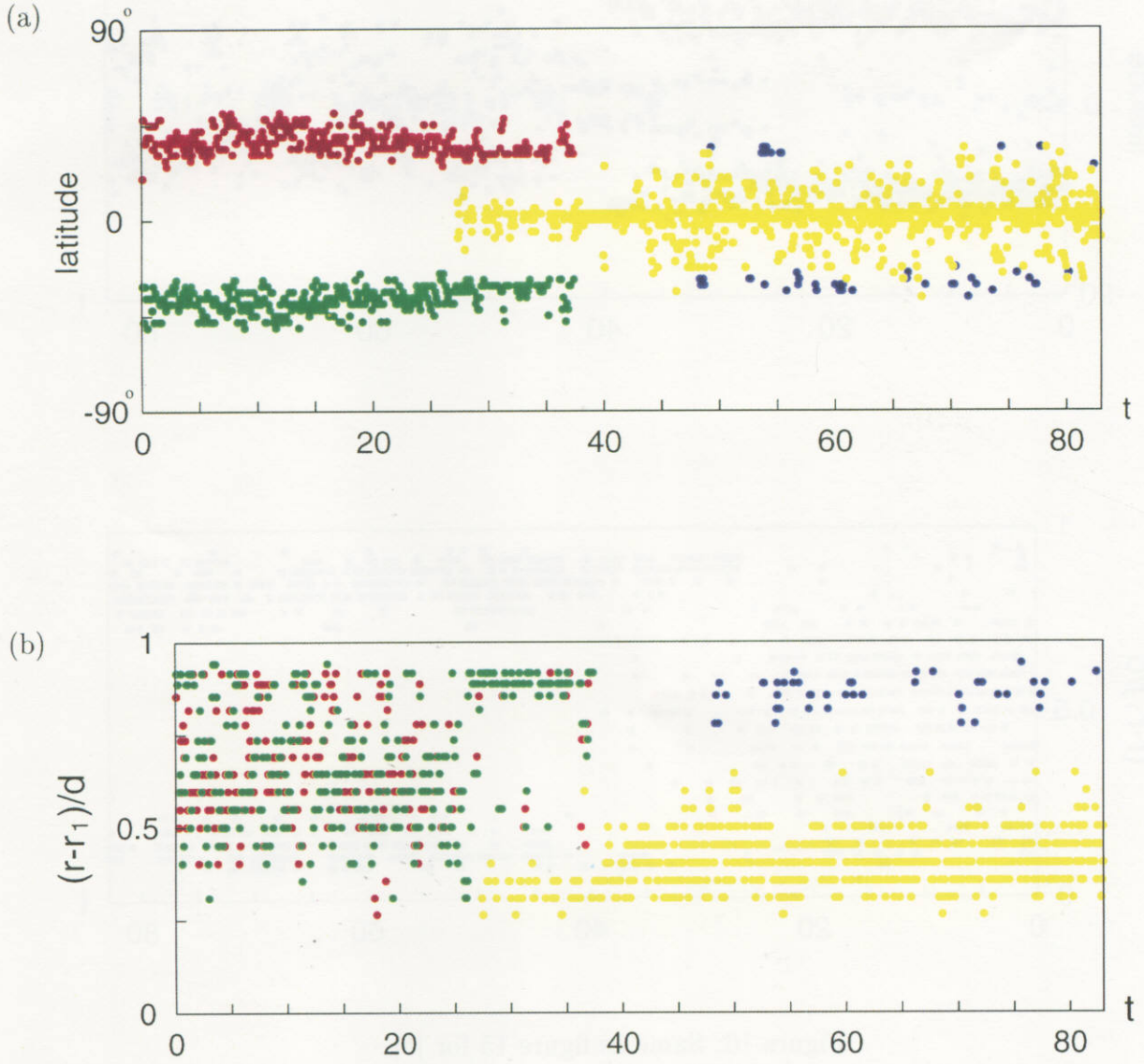

Figure 15: Location of the maximum of $|b_z|$. The maximum of $|b_z|$ is searched in each hemisphere separately. The location of the maximum is plotted with dots on (a) the latitudinal and (b) radial coordinates versus time plane. Colours distinguish the areas of locations of the maximums: Red and green refer to higher latitude than 20^o in the northern and southern hemispheres, respectively, at earlier times ($t < 40$), whereas dark blue, yellow, and light blue to the outer-sphere side ($r - r_1 > 0.7d$), the middle radial region ($0.3d < r - r_1 < 0.7d$), and the inner-sphere side ($r - r_1 < 0.3d$), respectively, in the whole time period except for the red and green areas.

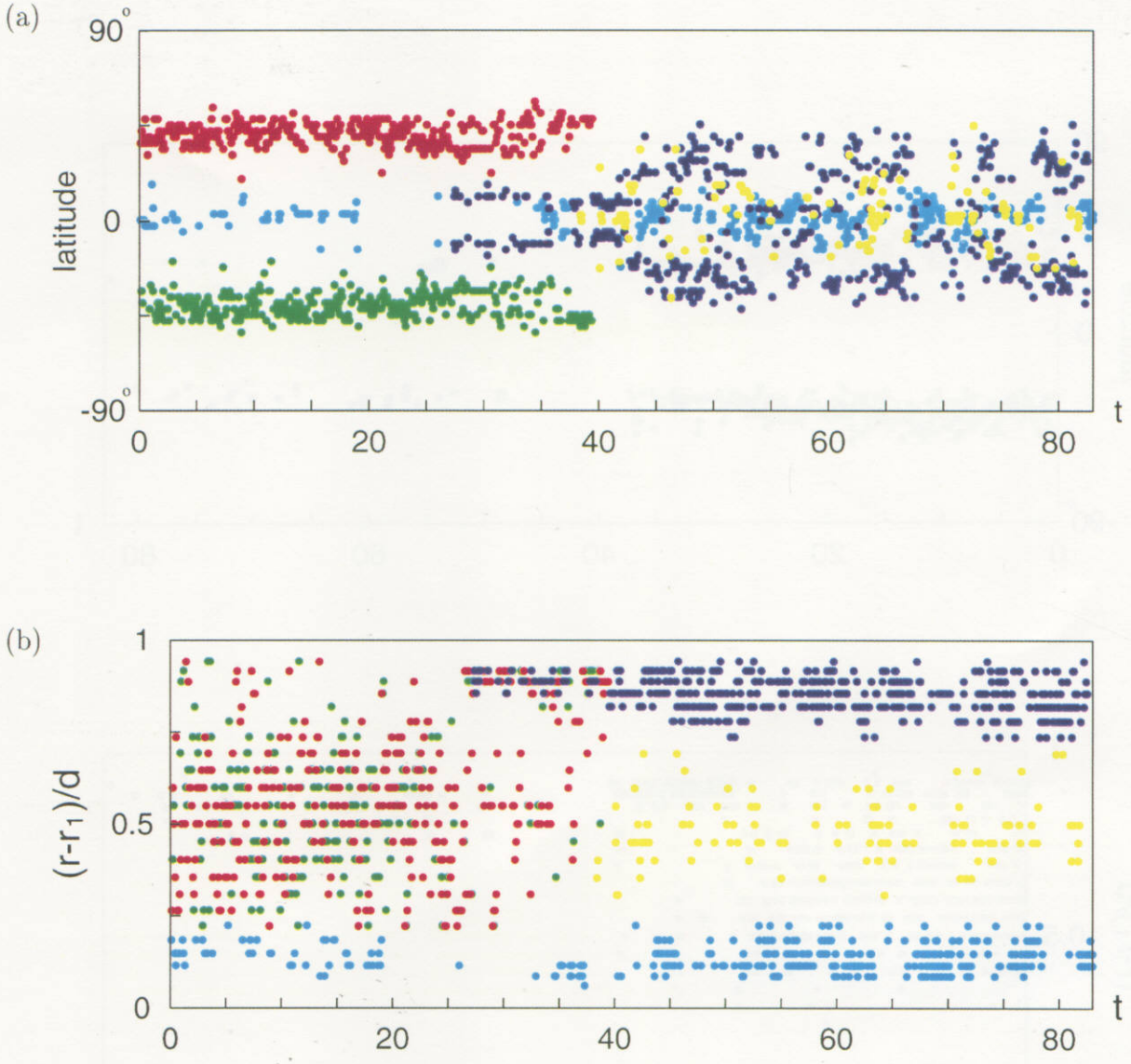

Figure 16: Same as figure 15 for $|\boldsymbol{b}|$.

in this period. Instead, another group of maximums (shown by dark blue) appear near the outer boundary ($r - r_1 > 0.78d$) and at low latitude ($30^o \pm 3^o$), which corresponds to the banana-shaped blobs (classified as $\langle c \rangle$ in Table 1) of strong magnetic field intensified along accelerating streamlines through the stagnation point just outside of the Ekman boundary layer along the outer sphere. It is interesting to note that these dark blue dots appear more in the periods of lower magnetic energy ($50 < t < 60$ and $70 < t < 80$), while they are very rare when the activity of the magnetic field is higher ($40 < t < 50$ and $60 < t < 70$) (see figure 2).

Although $|b_z|$ is the strongest component of the magnetic field in the present system, the other components are not negligible but play substantial roles in the dynamics. In figure 16, we plot the location of the maximum of $|\boldsymbol{b}|$ in the same manner as figure 15. These two figures show both similarity and difference. The red and green dots (classified as $\langle a \rangle$) in the linear

and first-equilibrium periods are commonly observed at similar places in the both figures. Also common are the groups of points appearing after around $t = 38.4$ which are plotted with yellow (classified as $\langle b \rangle$) and dark blue dots (classified as $\langle c \rangle$). Since the component not parallel to the rotation axis of the magnetic flux density in $\langle c \rangle$ is substantial, more dark blue dots are observed in figure 16. In contrast, light-blue dots are completely new in figure 16, which could not have been found without this plot. We classify this group as $\langle d \rangle$. These points are located near the inner core on the equatorial plane in which the component perpendicular to the rotation axis of the magnetic flux density is dominant. This is located between cyclones and their western neighbouring anti-cyclones (see the equatorial plane on the inner-sphere side in figures 13(b-iii), (b-ix)-(b-xi) and 14(b-iii), (b-v), (b-vi), (b-viii), (b-ix)). This is the same as that observed before in Kitauchi & Kida (1998) in the case of weak magnetic field, which is also generated by a concentrate-and-stretch of magnetic lines of force.

6 Competition between magnetic field and convection vortices

As seen in §5.3, there is an interesting dynamical competition between anti-cyclonic vortex blobs and the magnetic field which repeat cyclically in time. A single cycle is composed of three elementary processes, which are (i) the birth of convection vortices, (ii) the growth of anti-cyclones together with the intensification of magnetic field therein, and (iii) the break-down of anti-cyclones and the diminution of magnetic field. In the following we consider the dynamical mechanism in each of these processes separately.

6.1 Birth of Convection Vortices

First of all, we recall that there is a steady driving force by a temperature difference between the inner and outer spheres against the gravity force pointed to the system center. Since the cyclic process is repeated, it does not matter to begin with any step of the cycle. We start considering the birth of an anti-cyclone. Figure 17 is a typical time-series which show the birth of an anti-cyclone. Here, the velocity and magnetic fields are plotted on the equatorial plane. Time elapses from (a) to (d), which is a subdivision of the period between figures 13(vi) and (vii). Red lines with black dots represent streamlines, along which the fluid flows toward the dot. Vorticity distribution is depicted by contour lines with black for cyclones and white for anti-cyclones. Temperature distribution is represented by colour map with red for hotter areas and blue for cooler. There are five strong anti-cyclones in (a). All of them are wrapping high-temperature fluid blobs on their east side. Cyclones of much weaker intensity are accompanied with most of the anti-cyclones. The five anti-cyclones are more or less equally separated with each other. Notice, however, that the distance between anti-cyclones #5 and #6 is a bit longer than the others, and increases as time progresses from (b) to (d). In the meanwhile, high-temperature fluid blobs extend along the hot inner boundary, and at the same time a cyclone adjacent to anti-cyclone #6 grows. A new anti-cyclone #7 is born and grows

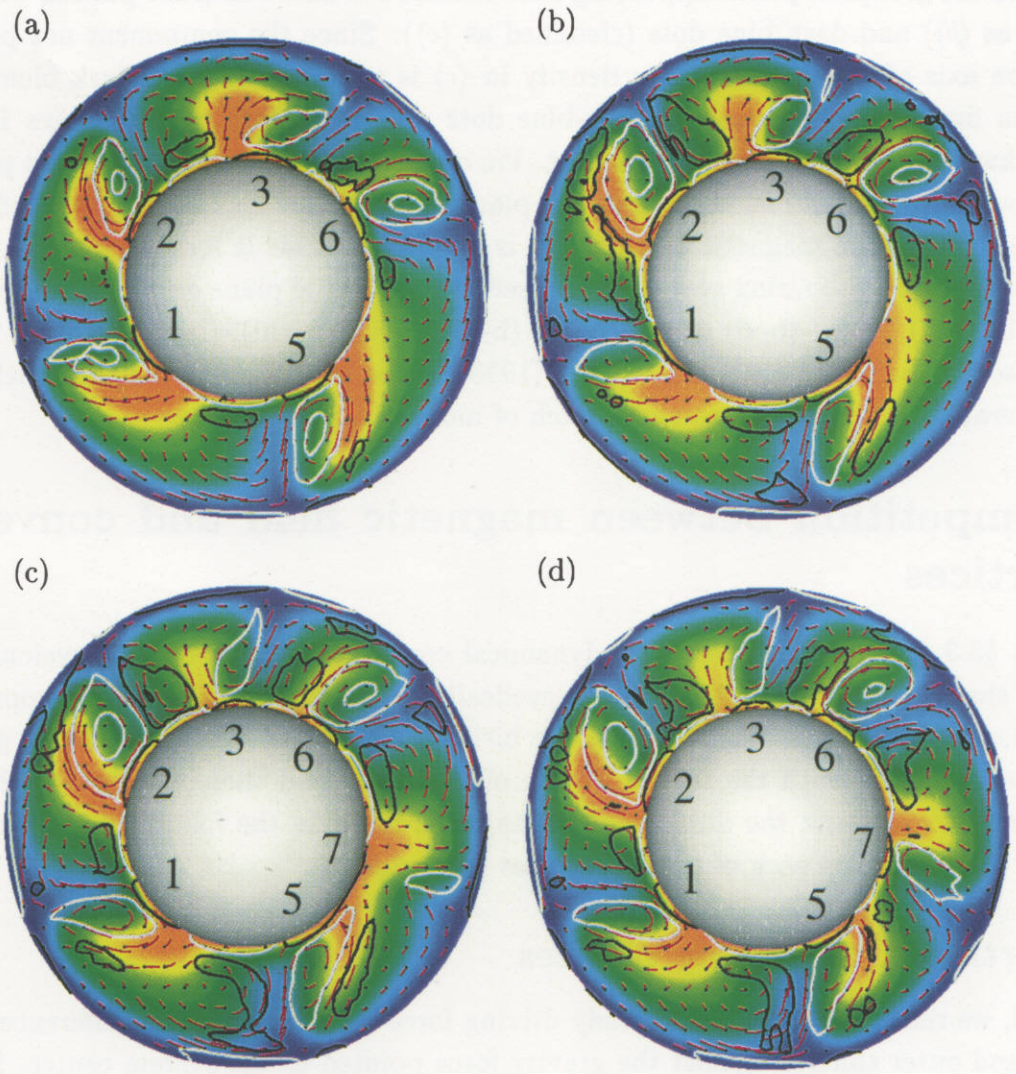

Figure 17: Birth of an anti-cyclone. Streamlines are represented on the equatorial annular plane by brown lines with black dots to which the flow is pointed. Vorticity contours are drawn with black for $\omega_z > 0$ and white for $\omega_z < 0$. Only a single value of the vorticity magnitude $|\omega_z|$ is chosen for the contours. Therefore, a double contour indicates the existence of a hollow at the center. The areas surrounded by contours are larger for anti-cyclones than for cyclones, implying that the former is stronger in intensity than the latter. Colour map shows the temperature distribution with red for hot areas and blue for cold. (a) $t = 58.7$, (b) 59.1, (c) 59.5, and (d) 59.6. Five cyclonic and anti-cyclonic swirling motions arrange alternatively over the annulus in (a). High-temperature blobs are pulled out from the inner boundary to the east side of each anti-cyclone. As time goes on, anti-cyclones #5 and #6 move away from each other, and a new high-temperature blob emanates in the middle, which creates a new anti-cyclone on the west side.

in (c) and (d). This is nothing but the Rayleigh-Bénard instability mechanism of thermal convection. Soon later, this new anti-cyclone grows to a strong one, whereas the neighbouring cyclone weakens (see figures 13(a-ix)-(a-xii)).

The same birth process of a new anti-cyclone is often observed. See, for example, the one numbered 6 in figure 13(a-ii), #8 in figure 14(a-i), #9 in figure 14(a-ii), and #10 in figure 14(a-iii). The one numbered 5 in figure 13(a-x) seems to have been generated in the same way as the above. Since, however, it was born at the place where a strong anti-cyclone was broken down (see #5 in figure 13(a-viii)), we assign the same number 5 to it.

6.2 Growth of anti-cyclones and intensification of magnetic field

It is observed in the second-equilibrium period that the anti-cyclones are much stronger in intensity than the cyclones. The primary cause of this inequality in intensity may be attributed to the Colioris force, which is pointed to (or away from) the center of anti-cyclones (or cyclones), and therefore the pressure tends to be higher (or lower) inside anti-cyclones (or cyclones). Since

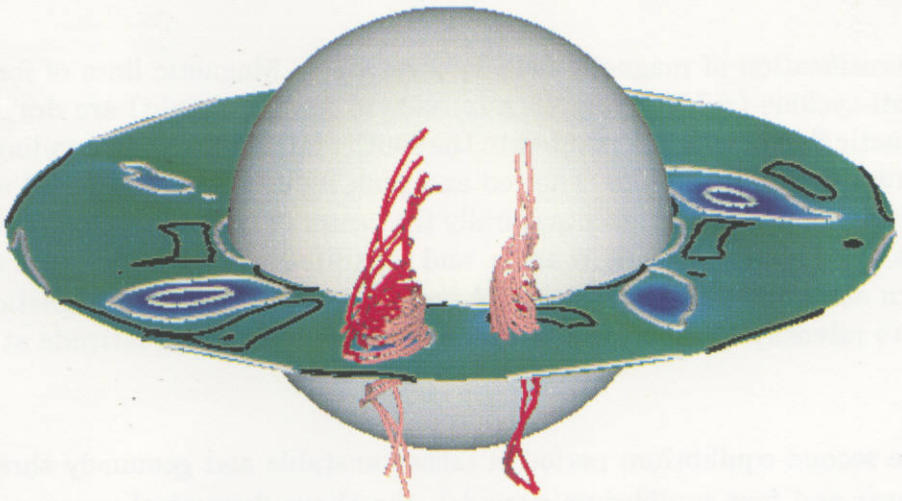

Figure 18: Helical streamlines around a cyclone and anti-cyclone. Streamlines (in the frame rotating with vortices) are drawn in the central regions of an anti-cyclone (which is #7 in figure 13(a-viii) viewed from the right) and its eastern neighbouring cyclone. Colour denotes the direction of velocity: Red for northward flows and pink for southward. There are helical motions both in a cyclone and in an anti-cyclone. The flow is pointed toward (or away from) the equatorial plane in the former (or the latter). The sense of rotation of the helical motion is like as a left-handed screw in the northern hemisphere both in the cyclone and anti-cyclone. Because of stretching (or shrinking) motions perpendicular to the equatorial plane in the anti-cyclone (or cyclone) the vorticity is intensified (or weakened) accordingly in the respective cases. Viewed from 20^o north latitude at $t = 60.5$.

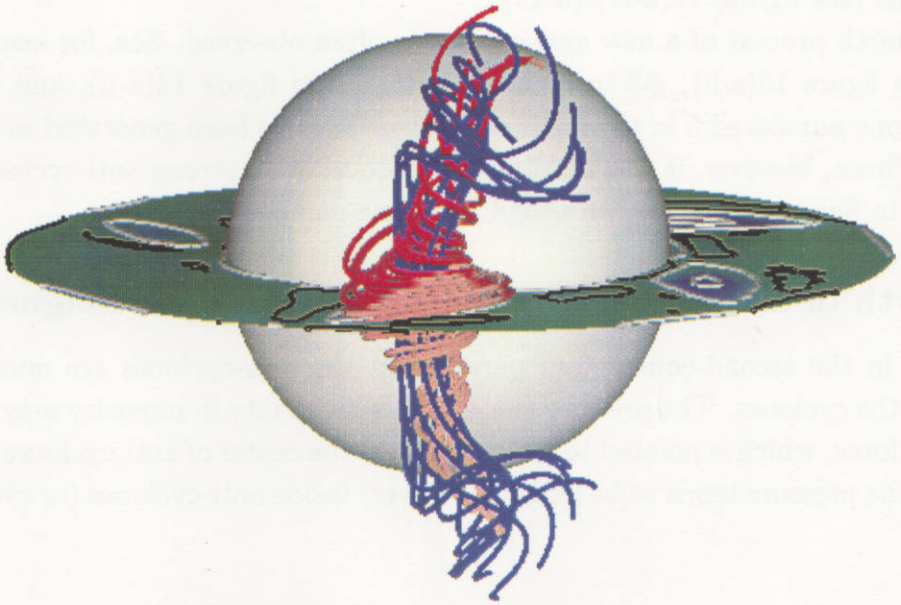

Figure 19: Intensification of magnetic field by stretching. Magnetic lines of force which pass through an anti-cyclone (#7 in figure 13(a-ix) viewed from the right) are drawn with purple lines, the magnetic flux of which is pointed to the south. Helical lines surrounding the magnetic lines of force represent streamlines. The red and pink indicate the northward and southward flows, respectively. The flow approaches spirally the center of the anti-cyclone on the equatorial plane, changes the direction by a right angle, and separates helically away from the plane both in the northern and southern hemispheres. Advected by this flow, the magnetic lines of force are stretched to intensify the magnetic field. Viewed from 10^o north-latitude at $t = 61.4$.

the flow in the second-equilibrium period is rather unstable and genuinely three-dimensional (unlike the linear and first-equilibrium periods), the above dynamical process is taking place mostly near the equatorial plane. Thus, the high-pressure blobs inside anti-cyclones flow to higher latitudes (i.e. away from the equatorial plane), and vice versa inside cyclones. This mechanism of inducing axial flow inside the convection vortices is different from that due to the Ekman pumping on the outer boundary which is applied to a quasi-two dimensional flow along the rotation axis of the spherical shell in the linear and first-equilibrium periods.

In order to see what is happening in the two kinds of oppositely rotating convection vortices, we plot, in figure 18, typical streamlines in an anti-cyclone (which is #7 in figure 13(viii)) and in its eastern neighbouring cyclone. Note that we are viewing figure 13(viii) from the right. Red and pink colours of streamlines denote northward and southward flows, respectively. There are helical motions of the same sense of helicity both in the anti-cyclone and cyclone. The flow is pointed to the equatorial plane in the cyclone, whereas it is away from in the anti-cyclone. As a result, the vorticity lines inside the cyclone (or anti-cyclone) are being shrinked (or stretched)

to weaken (or intensify) the strength of vorticity. This self-growing process is taking place in all the anti-cyclones, which is also accompanied with the intensification of magnetic field as described below.

Anti-cyclones draw fluid elements spirally into themselves in the equatorial plane and blow them up along their rotating axes helically. Advected by this flow, the magnetic lines of force are gathered at the center of anti-cyclones on the equatorial plane and stretched along their rotation axes. In figure 19, we plot streamlines around an anti-cyclone (which is #7 in figure 13(a-ix)) with red-and-pink lines together with magnetic field lines (purple lines) which pass through the central region of the anti-cyclone. It is seen that the magnetic flux is transported toward the center along the equatorial plane, which is then stretched in the direction perpendicular to the equatorial plane. This concentrate-and-stretch of magnetic field lines is observed in every anti-cyclone and should be the main mechanism of the magnetic field intensification (Kidauchi & Kida 1998).

6.3 Break-down of anti-cyclones and diminution of magnetic field

As discussed in the preceding section the magnetic field is intensified by stretching of magnetic field lines of force inside anti-cyclones. But it can not continue forever. The intensified magnetic field concentrated in a tube region induces electric current around it by the Ampère law which couples with the surrounding magnetic field to generate the Lorentz force in the outward radial direction. As a result, the flow toward the center of anti-cyclones is weakened and even reversed the direction to lead to breakdown of the anti-cyclones, and the magnetic field faints away because it loses the support.

The situation that anti-cyclones having strong magnetic field in them are suffering from the Lorentz force directed to the outward radial directions is shown in figure 20, which is a snapshot at $t = 62.3$. Here, the lines of Lorentz force are drawn on the equatorial plane by red lines with a dot to which the Lorentz force is pointed. Convection vortices are shown by contours of ω_z with black for cyclones and white for anti-cyclones. Only a single level of $|\omega_z|$ are drawn here so that a double contour implies the existence of a hollow at the center. The colour map represents the distribution of the z component of magnetic field with red for $b_z > 0$ and blue for $b_z < 0$. At this time all the anti-cyclones happen to have negative b_z, whereas positive one is hardly seen. There are four double-contour anti-cyclones having strong magnetic field in them. The Lorentz force is very strong inside these anti-cyclones and pointed to the outward radial directions. We can also see that the Lorentz force is pointed to the inward in cyclones represented by black lines. Similar behaviours are observed on other planes $z = const.$ parallel to the equatorial plane at least where $|z| < 1$.

At the place where an anti-cyclone has broken down and the magnetic field has disappeared only weak random fluctuations of vorticity and magnetic flux are left. Thereafter, sooner or later, a new anti-cyclone is created by the Rayleigh-Bénard instability (see §6.1), and the dynamical process will be repeated.

This stage of the birth of a new convection vortex may have a key ingredient with relation

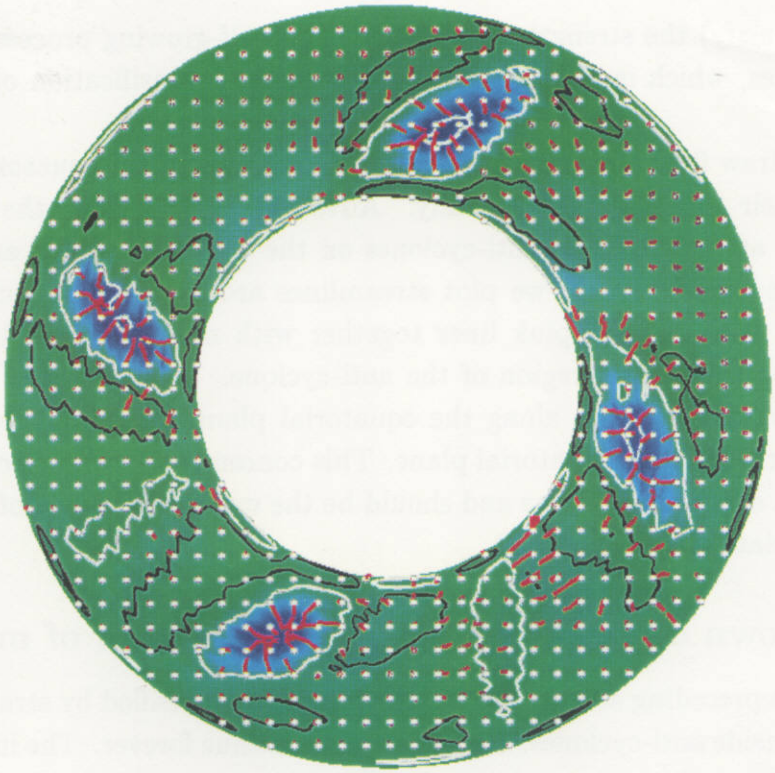

Figure 20: Lines of Lorentz force. Red lines with a white dot represent the lines of Lorentz force directed to the dot. The z component of vorticity is shown by contours with black for cyclones and white for anti-cyclones. The magnitude of all the contours is same so that a double contour of an anti-cyclone indicate a hollow at the center. Colour map represents the z component of magnetic field with red (hardly seen) for $b_z > 0$ and blue for $b_z < 0$. This equatorial plane is viewed from the north at $t = 62.3$.

to the magnetic field reversal. This is because the direction of the grown magnetic field may be determined by an accidental sign of a random weak magnetic field. Since the remnant of previous magnetic field has some influence to determine the next sign, some violent event of substantial strength may be necessary to change the sign. This scenario is not observed in the present numerical simulation, but it is possible to occur in a longer run.

7 Concluding Remarks

The convection dynamo in a rotating spherical shell has been investigated numerically and visually with the aim of finding a mechanism of magnetic field intensification. An electrically conducting Boussinesq fluid is confined in a spherical shell which rotates with constant angular velocity. The temperature on the inner and outer spherical boundaries are fixed to be uniform and constant at all times. The inner sphere is hotter than the outer, which drives a thermal convection against a gravity force pointed to the system center. The non-slip boundary condition is imposed for the velocity. The magnetic field is connected smoothly on the

boundaries with potential fields in vacuum outside the spherical shell. The initial condition of the MHD simulation is given by a random weak magnetic seed on a statistically stationary thermal convection at the Rayleigh number double the critical. This is one of the simplest nontrivial dynamical models (which retain three fundamental factors, i.e. the system rotation, the spherical boundaries, and the convective motion of an electrically conducting fluid) for realization of self-sustained magnetic fields observed in many of celestial bodies. The following scenario of magnetic field intensification has been observed at the Roberts number of 0.68 times the critical.

The purely thermal convection before imposing the magnetic field is composed of nine (this number should change depending on the control parameters) pairs of cyclonic and anti-cyclonic convection vortices which are stretched along the rotation axis and retrograde with a nearly constant angular velocity. In the initial stage of evolution when the magnetic field is still weak in intensity, the vortex columns are two-dimensional and robust. The magnetic field is intensified predominantly between cyclones and their western neighbouring anti-cyclones at middle latitude, where the stretching rate of the convection velocity field is maximum. The intensity of the magnetic field increases exponentially in time. This is called the linear period. Before long, the magnetic field grows strong enough to alter the convection velocity field through the Lorentz force. Then the two-dimensional vortex columns are deformed, the maximum stretching rate is reduced, and the intensification mechanism in the above-mentioned place stops. On the other hand, the concentrate-and-stretch mechanism of magnetic lines of force keeps going inside anti-cyclones. The growth rate of the magnetic field there is not so large to break down the vortex columns. This is the first-equilibrium period. Thereafter, sooner or later, the magnetic field develops to be strong enough to destroy anti-cyclones. Then, the number of anti-cyclones decreases to $4 \sim 6$, a half of the initial number 9. This is the second-equilibrium period, in which three sequential dynamical processes repeat. That is, the birth of the convection vortices through the Rayleigh-Bénard instability, the growth of anti-cyclones and the intensification of magnetic field therein by concentrate-and-stretch mechanism, and the break-down of anti-cyclones through the Lorentz force induced by the intensified magnetic field. The transfer of magnetic energy to the kinetic is taking place mostly in this recurrent cycle of creation-and-annihilation of convection vortices and magnetic field. It is interesting to see that the dissipation rates of the kinetic and the magnetic energy are almost equal throughout the second-equilibrium period. Incidentally, there is no strong magnetic field observed inside the Ekman boundary layer in spite of strong shearing motions there. This is because the resistive dissipation is also large to compensate it.

Because of complexity of the spatiotemporal behaviour of velocity and magnetic fields their longitudinal averages have often been investigated as a simplified surrogate of the full three-dimensional structure. As we have seen in this paper, however, the fields are far from axi-symmetric and the dynamo action is a non-axi-symmetric local phenomenon. A correct dynamo mechanism could be identified only by looking hard at local instantaneous structures of the velocity and magnetic fields. For example, a banana-shaped blob of intense magnetic field always appears together with a cigar-shape inside an anti-cyclone in the above recurrent

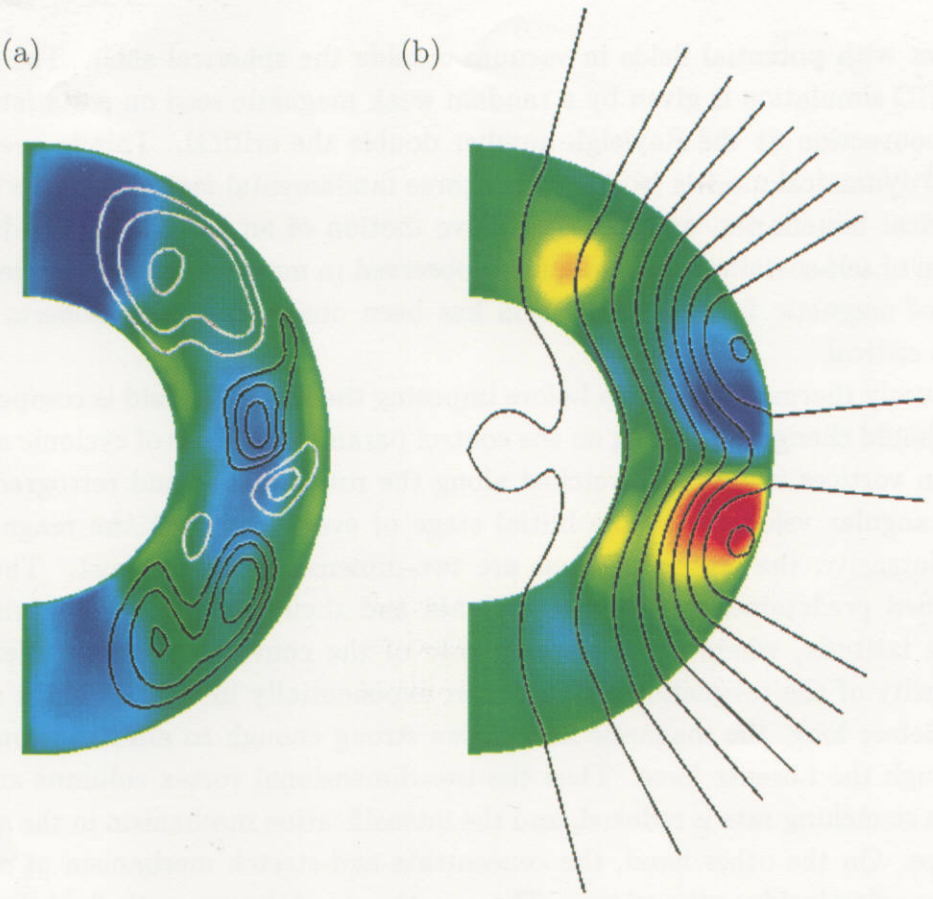

Figure 21: Longitudinal averaged structure of velocity and magnetic fields in a meridional plane. (a) Velocity field. The meridional component of velocity is represented by streamlines with white for clockwise rotation and black for counter-clockwise rotation. Colour map denotes the angular velocity relative to the mean value over the whole spherical shell with red for positive (eastward) and blue for negative (westward). (b) Magnetic field. Black lines shows the meridional (poloidal) component of magnetic lines of force which is pointed to the south (downward). The longitudinal (toroidal) component is represented by colour map with red for positive and blue for negative. There is no longitudinal component in vacuum outside the spherical shell. $t = 64.1$.

dynamical process. These two blobs are connected to make a 'twist-turn' loop of intense magnetic flux density. This unique loop constitutes a key structure in the sense that it gives the main contribution, after a longitudinal averag, to a commonly observed dipole pattern of the poloidal components of the magnetic field and bull's-eyes pattern of the toroidal component.

In figures 21, we plot the longitudinal average of (a) the velocity and (b) magnetic fields at some time instant in the second-equilibrium period. The longitudinal and meridional components are shown on a meridional plane with colour map and lines, respectively. We see, in these figures, the well-known characteristics of the axi-symmetric components of the velocity and magnetic fields: [1] There is a differential rotation in which the flow near the rotation axis prograde faster on the equatorial plane. [2] The toroidal magnetic field has a pair of strong peaks of opposite sense at low latitude near the outer boundary, and another pair of

weaker peaks near the rotation axis. [3] The poroidal magnetic field shows a dipole structure (see Sakuraba & Kono 1999, Christensen, Olson & Glatzmaier 1999). It is a common practice that the conversion (ω effects) from the poloidal to toroidal components of magnetic lines of force is explained by a differential rotation in the longitudinal averaged velocity. We should note, however, how it is difficult to imagine an instantaneous local structure of the velocity and magnetic fields from the longitudinal averages. This gives us a warning that the argument of the α and/or β dynamo based on only the longitudinal average may not be able to capture the true dynamics of local nature.

There remain several interesting questions on behaviour of the generation mechanism and structure of the magnetic field. First, why is the magnetic field intensified much more in the second-equilibrium period than in the first ? We note there are two important differences in the structure of anti-cyclones between the first- and second-equilibrium periods. That is, in the latter, the number of anti-cyclones is decreased by half, and the two-dimensional structure is broken down, and the vorticity is localized near the equatorial plane. These changes may work to strengthen the intensity of anti-cyclones themselves and also the magnetic field. Secondly, how is a reversal of the dipole polarity possible ? Although no reversal observed in the present numerical simulation, there is a possible trigger of the reversal. It is the unpredictable direction of weak magnetic flux density near the equatorial plane just after an anti-cyclone is broken down and the magnetic field associated with it diminishes in the recurrent cycle of creation-and-annihilation of convection vortices and magnetic field. Thirdly, how general are the mechanisms of magnetic field intensification observed in the present numerical simulation ? Variant appearances of the convection field structure depending on the control parameters make us inclined to suppose that there may be many different mechanisms. The stretching of magnetic lines of force is the only mechanism of the magnetic field intensification, though. A comparison of many studies by different authors suggests that the concentrate-and-stretch of magnetic lines of force, especially in anti-cyclones, seems to be a common dynamo mechanism (Kageyama & Sato 1997, Olson, Christensen & Glatzmaier 1999, Katayama, Matsushita & Honkura 1999, Sakuraba & Kono 1999). It should not forget, however, to note that there are two completely different types of flow structure of thermal convection depending on the magnitude of the Rayleigh number. The convection inside the imaginary tangent cylinder (a circular cylinder parallel to the rotation axis and tangent to the inner sphere) is more active than the outside if the Rayleigh number exceeds some critical value (Glatzmaier & Roberts 1995, 1997; Olson, Christensen & Glatzmaier 1999). Accordingly, their magnetic field is intensified more inside the tangent cylinder than the outside, which is completely different from the one realized by the present numerical simulation. It is one of the interesting challenging problems whether there is any unified dynamo mechanism applied both inside and outside the tantentical cylinder.

This work has been supported by the Grant-in-Aid for Scientific Research on Priority Areas (B) from the Ministry of Education, Culture, Sports, Science and Technology of Japan.

References

Busse, F.H. 2000 Homogeneous Dynamos in Planetary Cores and in the Laboratory. *Annu. Rev. Fluid Mech.* **32**, 383-408.

Christensen, U., Olson, P. & Glatzmaier, G.A. 1999 Numerical modelling of the geodynamo: a systematic parameter study. *Geophys. J. Int.* **138**, 393-409.

Glatzmaier, G.A. & Roberts, P.H. 1995 A three dimensional self-consistent computer simulation of a geomagnetic field reversal. *Nature* **377**, 203-209.

Glatzmaier, G.A. & Roberts, P.H. 1996 An anelastic evolutionary geodynamo simulation driven by compositional and thermal convection. *Physica D* **97**, 81-94.

Glatzmaier, G.A. & Roberts, P.H. 1997 Simulating the geodynamo. *Contemp. Phys.* **38**, 269-288.

Gubbins, D. & Bloxham, J. 1987 Morphology of the geomagnetic field and implications for the geodynamo, *Nature* **325**, 509-513.

Hollerbach, R. & Jones, C.A. 1995 On the magnetically stabilizing role of the Earth's inner core. *Phys. Earth Planet. Int.* **87**, 171-181.

Ishihara, N. & Kida, S. 2000 Axial and equatorial magnetic dipoles generated in a rotating spherical shell. *J. Phys. Soc. Jpn.* **69**, 1582-1585.

Kageyama, A. & Sato, T. 1997 Generation mechanism of a dipole field by a magnetohydrodynamic dynamo. *Phys. Rev. E* **55**, 4617-4626.

Katayama, J.S., Matsushima, M. & Y. Honkura 1999 Some characteristics of magnetic field behavior in a model of MHD dynamo thermally driven in a rotating spherical shell. *Phys. Earth Planet. Inter.* **111**, 141-159.

Kida, S. Araki, K. & Kitauchi, H. 1997 Periodic reversals of magnetic field generated by thermal convection in a rotating spherical shell. *J. Phys. Soc. Jpn.* **66**, 2194-2201.

Kida, S. & Kitauchi, H. 1998a Chaotic reversals of dipole moment of thermally driven magnetic field in a rotating spherical shell. *J. Phys. Soc. Jpn.* **67**, 2950-2951.

Kida, S. & Kitauchi, H. 1998b Thermally driven MHD dynamo in a rotating spherical shell. *Prog. Theor. Phys. Suppl.* **130**, 121-136.

Kitauchi, H., Araki, K. & Kida, S. 1997 Flow structure of thermal convection in a rotating spherical shell. *Nonlinearity* **10**, 885-904.

Kitauchi, H. & Kida, S. 1998 Intensification of magnetic field by concentrate-and-stretch of magnetic flux lines. *Phys. Fluids* **10**, 457-468.

Kuang, W. & Bloxham, J. 1997 An earth-like numerical dynamo model. *Nature* **389**, 371-374.

Larmor, J. 1919 How could a rotating body such as the sun become a magnet ? *Rep. Brit. Assoc. Adv. Sci.* 159-160.

Merril, R.T., McElhinny, M.W. & McFadden, P.L 1996 *The Magnetic Field of the Earth, Paleomagnetism, the Core, and the Deep Mantle.* (Academic Press, San Diego).

Olson, P., Christensen, J. & Glatzmaier, G. A. 1999 Numerical modeling of the geodynamo: mechanisms of field generation and equilibration. *J. Geophys. Res.* **104**, 10,383-404.

Roberts, P.H. & Glatzmaier, G.A. 2000 Geodynamo theory and simulations. *Rev. Mod. Phys.* **74**, 1081-1123.

Roberts, P.H. & Soward, A.M. Soward 1992 Dynamo theory. *Annu. Rev. Fluid Mech.* **24**, 459-512.

Sakuraba, A. & Kono, M. 1999 Effect of the inner core on the numerical solution of the magnetohydrodynamic dynamo. *Phys. Earth Planet. Inter.* **111**, 105-121.

Zhang, K.-K. & Schubert, G. 2000 Magnetohydrodynamics in rapidly rotating spherical systems. *Annu. Rev. Fluid Mech.* **32**, 409-443.

Recent Issues of NIFS Series

NIFS-682 H Momota and G H Miley
Virtual Cathode in a Spherical Inertial Electrostatic Confinement Device Feb 2001

NIFS-683 K Saito, R Kumazawa, T Mutoh, T Seki T Watari, Y Torii, D A Hartmann Y Zhao A Fukuyama F Shimpo, G Nomura M Yokota, M Sasao, M Isobe, M Osakabe T Ozaki, K Narihara Y Nagayama S Inagaki, K Itoh, S Morita, A V Krasilnikov K Ohkubo, M Sato, S Kubo, T Shimozuma, H Idei Y Yoshimura, O Kaneko Y Takeiri, Y Oka, K Tsumori K Ikeda, A Komori, H Yamada, H Funaba, K Y Watanabe, S Sakakibara M Shoji, R Sakamoto, J Miyazawa, K Tanaka, B J Peterson N Ashikawa, S Murakami, T Minami, S Ohakachi, S Yamamoto, S Kado, H Sasao, H Suzuki K Kawahata, P deVries, M Emoto, H Nakanishi, I Kobuchi, N Inoue, N Ohyabu, Y Nakamura S Masuzaki, S Muto, K Sato, T Morisaki, M Yokoyama, T Watanabe, M Goto, I Yamada, K Ida T Tokuzawa, N Noda, S Yamaguchi, K Akaishi A Sagara, K Toi K Nishimura, K Yamazaki, S Sudo Y Hamada, O Motojima, M Fujiwara,
Ion and Electron Heating in ICRF Heating Experiments on LHD Mar 2001

NIFS-684 S Kida and S Goto,
Line Statistics Stretching Rate of Passive Lines in Turbulence Mar 2001

NIFS-685 R Tanaka, T Nakamura and T. Yabe,
Exactly Conservative Semi-Lagrangian Scheme (CIP-CSL) in One-Dimension Mar 2001

NIFS-686 S. Toda and K Itoh,
Analysis of Structure and Transition of Radial Electric Field in Helical Systems Mar 2001

NIFS-687 T Kuroda and H Sugama,
Effects of Multiple-Helicity Fields on Ion Temperature Gradient Modes Apr 2001

NIFS-688 M Tanaka,
The Origins of Electrical Resistivity in Magnetic Reconnection Studies by 2D and 3D Macro Particle Simulations Apr 2001

NIFS-689 A Maluckov, N Nakajima, M Okamoto, S Murakami and R Kanno,
Statistical Properties of the Neoclassical Radial Diffusion in a Tokamak Equilibrium Apr 2001

NIFS-690 Y Matsumoto, T Nagaura, Y Itoh, S-I Oikawa and T Watanabe,
LHD Type Proton-Boron Reactor and the Control of its Peripheral Potential Structure Apr 2001

NIFS-691 A Yoshizawa, S -I Itoh, K Itoh and N Yokoi,
Turbulence Theories and Modelling of Fluids and Plasmas Apr 2001

NIFS-692 K Ichiguchi, T Nishimura, N Nakajima, M Okamoto, S -i Oikawa, M Itagaki,
Effects of Net Toroidal Current Profile on Mercier Criterion in Heliotron Plasma Apr 2001

NIFS-693 W Pei, R. Horiuchi and T. Sato,
Long Time Scale Evolution of Collisionless Driven Reconnection in a Two-Dimensional Open System: Apr 2001

NIFS-694 L N Vyachenslavov, K. Tanaka, K Kawahata,
CO2 Laser Diagnostics for Measurements of the Plasma Density Profile and Plasma Density Fluctuations on LHD Apr. 2001

NIFS-695 T Ohkawa,
Spin Dependent Transport in Magnetically Confined Plasma May 2001

NIFS-696 M Yokoyama, K. Ida, H Sanuki, K Itoh, K Narihara, K Tanaka, K Kawahata, N Ohyabu and LHD experimental group
Analysis of Radial Electric Field in LHD towards Improved Confinement May 2001

NIFS-697 M Yokoyama, K. Itoh, S. Okamura, K Matsuoka, S. -I Itoh,
Maximum-J Capability in a Quasi-Axisymmetric Stellarator May 2001

NIFS-698 S-I Itoh and K Itoh,
Transition in Multiple-scale-lengths Turbulence in Plasmas May 2001

NIFS-699 K. Ohi, H. Naitou, Y. Tauchi, O Fukumasa,
Bifurcation in Asymmetric Plasma Divided by a Magnetic Filter May 2001

NIFS-700 H Miura, T. Hayashi and T Sato,
Nonlinear Simulation of Resistive Ballooning Modes in Large Helical Device June 2001

NIFS-701 G Kawahara and S Kida,
A Periodic Motion Embedded in Plane Couette Turbulence June 2001

NIFS-702 K. Ohkubo,
Hybrid Modes in a Square Corrugated Waveguide. June 2001

NIFS-703 S.-I Itoh and K Itoh,
Statistical Theory and Transition in Multiple-scale-lengths Turbulence in Plasmas June 2001

NIFS-704 S. Toda and K Itoh,
Theoretical Study of Structure of Electric Field in Helical Toroidal Plasmas June 2001

NIFS-705 K Itoh and S-I Itoh,
Geometry Changes Transient Transport in Plasmas June 2001

NIFS-706 M Tanaka and A. Yu Grosberg
Electrophoresis of Charge Inverted Macroion Complex Molecular Dynamics Study July 2001

NIFS-707 T-H Watanave H Sugama and T Sato
A Nondissipative Simulation Method for the Drift Kinetic Equation July 2001

NIFS-708 N Ishihara and S Kida,
Dynamo Mechanism in a Rotating Spherical Shell Competition between Magnetic Field and Convection Vortices July 2001